SpaCeFormer: Fast Proposal-Free Open-Vocabulary 3D Instance Segmentation

Chris Choy [1] **Junha Lee** [2] **Chunghyun Park** [2] **Minsu Cho** [2] **Jan Kautz** [1]

Abstract

Open-vocabulary 3D instance segmentation is a core capability for robotics and AR/VR, but prior methods trade one bottleneck for another: multi-stage 2D+3D pipelines aggregate foundation-model outputs at hundreds of seconds per scene, while pseudo-labeled end-to-end approaches rely on fragmented masks and external region proposals. We present SpaCeFormer, a proposal-free space-curve transformer that runs at 0.14 seconds per scene, 2–3 orders of magnitude faster than multi-stage 2D+3D pipelines. We pair it with SpaCeFormer-3M, the largest open-vocabulary 3D instance segmentation dataset (3.0M multi-view-consistent captions over 604K instances from 7.4K scenes) built through multi-view mask clustering and multi-view VLM captioning; it reaches **21× higher mask recall** than prior single-view pipelines (54.3% vs 2.5% at IoU>0.5). SpaCeFormer combines spatial window attention with Morton-curve serialization for spatially coherent features, and uses a RoPE-enhanced decoder to predict instance masks directly from learned queries without external proposals. On ScanNet200 we achieve 11.1 zero-shot mAP, a 2.8× improvement over the prior best proposal-free method; on ScanNet++ and Replica, we reach 22.9 and 24.1 mAP, surpassing all prior methods including those using multi-view 2D inputs.

1. Introduction

Understanding 3D scenes with open-vocabulary descriptions is fundamental for autonomous driving (Zhang et al., 2024), augmented reality (Guo et al., 2024), and embodied AI (Rashid et al., 2023; Driess et al., 2023). Unlike closed-set 3D segmentation (Qi et al., 2017; Choy et al., 2019; Schult et al., 2023) that assumes a fixed label space, open-vocabulary 3D segmentation aims to identify and segment arbitrary objects described in natural language (Peng et al., 2023). This capability is crucial in real-world environments where the long-tail of object types far exceeds any predefined taxonomy (Liu et al., 2019).

While end-to-end 3D approaches would be ideal, the lack of large-scale 3D-text paired data remains a fundamental barrier for training open-vocabulary 3D instance segmentation models (Yang et al., 2024a). This challenge has driven research along two parallel directions: (1) multi-stage inference pipelines that aggregate 2D foundation model (Kirillov et al., 2023; Radford et al., 2021) proposals into 3D (Takmaz et al., 2023; Nguyen et al., 2024; Yin et al., 2024), and (2) using 2D models to generate pseudo-labeled 3D-text datasets for training end-to-end networks (Luo et al., 2024; 2023; Jia et al., 2024; Yang et al., 2024b; Lee et al., 2025a).

Multi-stage inference pipelines suffer from compounding errors across stages, dataset-specific thresholds that limit generalization, and substantial inference latency from sequential proposal processing, often hundreds of seconds per scene (Fig. 1). Pseudo-labeling approaches offer end-to-end learning, but existing methods rely on single-view captioning that produces inconsistent descriptions, and lifting 2D outputs to 3D yields fragmented instances due to occlusion. Open-vocabulary instance segmentation also demands spatially coherent features to distinguish fine-grained object boundaries across arbitrary categories, and existing 3D backbones prioritize efficiency over spatial coherence: architectures like Point Transformer (Wu et al., 2024) and OctFormer (Wang, 2023) serialize point clouds via space-filling curves, scattering spatially adjacent points across attention windows, making it difficult to capture the sharp, instance-level boundaries necessary for generalizing to novel object types.

To address these limitations in pseudo-labeled dataset construction and 3D backbone design, we introduce SpaCeFormer-3M, a large-scale open-vocabulary 3D instance segmentation dataset constructed via multi-view mask clustering and captioning, and SpaCeFormer (**Spa**ce-**C**urv**e** Trans**former**), an end-to-end network architecture tailored for open-vocabulary 3D instance segmentation. Our key insight is that multi-view consistency, both in mask

[1]NVIDIA [2]POSTECH. Correspondence to: Chris Choy <cchoy@nvidia.com>.

Preprint. April 17, 2026.

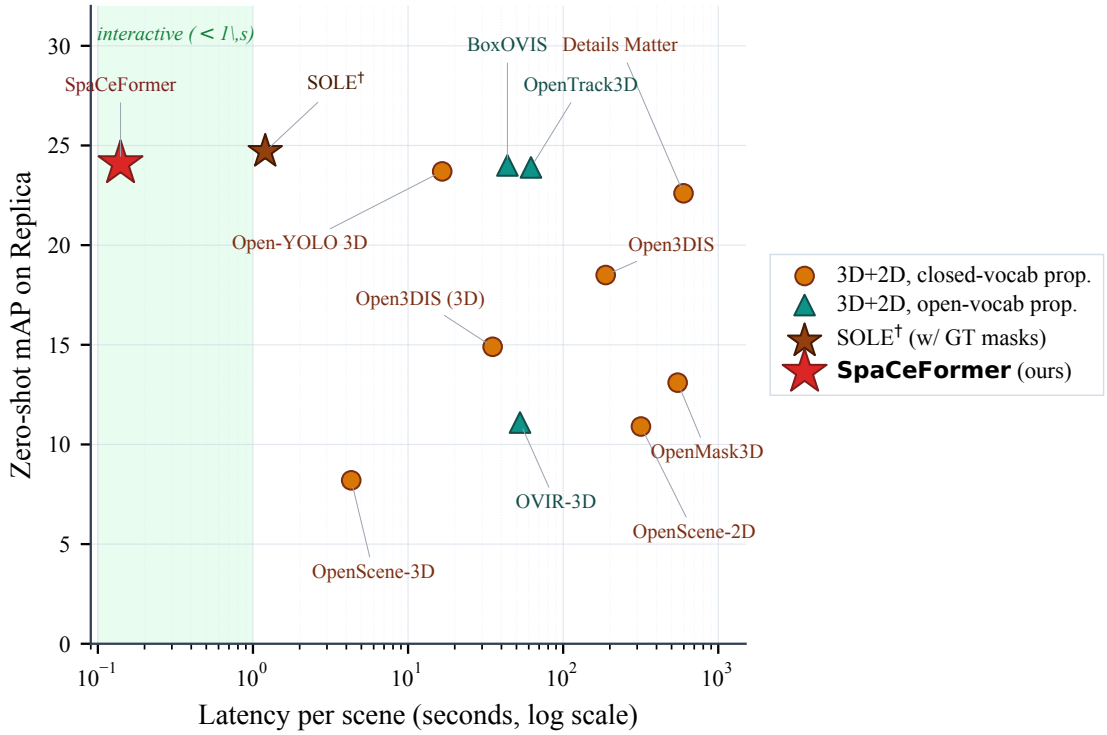

Figure 1. **Accuracy vs. latency on Replica zero-shot open-vocabulary 3D instance segmentation.** SpaCeFormer (red star) reaches **24.1 mAP at 0.14 s per scene**: Pareto-optimal among methods that use no GT 3D supervision, and **2–3 orders of magnitude faster** than multi-stage 2D+3D pipelines while using only 3D input (no 2D RGB-D streams, no external region proposals). SOLE is the only method above us on mAP (24.7), but requires ScanNet200 ground-truth mask supervision and is ∼9× slower. SpaCeFormer is the only method that enters the "interactive" band (<1 s, shaded). Latency on a log scale; see Table 3 for full numbers. †SOLE's latency is estimated from its Mask3D backbone.

aggregation and captioning, combined with spatially coherent 3D features enables effective proposal-free instance segmentation without multi-stage heuristics.

On the data side, we address two key limitations of RegionPLC (Yang et al., 2024b) and Mosaic3D (Lee et al., 2025a): fragmented masks and inconsistent captions caused by single-view processing. We aggregate partial 2D masks into complete, geometry-consistent 3D instances via multi-view mask clustering (Yan et al., 2024), and employ multi-view prompting to produce view-consistent descriptions. The resulting dataset, SpaCeFormer-3M (3.0M multi-view-consistent captions over 604K instance masks across 7.4K scenes), has significantly higher mask completeness and caption consistency than prior pseudo-label corpora: **54.3% mask recall at IoU>0.5** on ScanNet versus 2.5% for single-view pipelines like Mosaic3D, a 21× improvement (Sec. 3). Geometry-consistent training data is essential for our proposal-free architecture: the decoder must learn to predict complete instance masks from spatially coherent features, which requires training on complete, non-fragmented mask annotations.

On the modeling side, SpaCeFormer builds on Point Transformer v3 (Wu et al., 2024) with a new attention design: *space-curve attention*, which combines spatial window attention with Morton curve serialization. Each component exists in prior work, but their combination is novel and specifically motivated by our proposal-free setting. Spatial windows preserve coherent local neighborhoods that matter for instance boundary prediction (achieving 28.6% lower intra-window spatial distance than Morton-only attention), while Morton curves provide structured diversity at coarser scales. Together with 3D RoPE (Su et al., 2024) in both backbone and decoder, these features support proposal-free mask prediction via learned queries (Carion et al., 2020; Cheng et al., 2022) without multi-stage heuristics.

We evaluate SpaCeFormer on three benchmarks for open-vocabulary 3D instance segmentation. On Replica, SpaCeFormer reaches **24.1 zero-shot mAP at 0.14 s per scene**, the only open-vocabulary method that operates at interactive rates; in accuracy it is matched only by SOLE (Lee et al., 2025b) (24.7 mAP), which requires ScanNet200 ground-truth mask supervision and is ∼9× slower (Fig. 1, Tab. 3). On ScanNet200 (Tab. 5), under the matched regime of *proposal-free, 3D-only input, no GT 3D annotations*, SpaCeFormer attains 11.1 mAP at 0.14 s per scene, 2.8× over the next-best method in this regime (Mosaic3D+Decoder, 3.9

mAP). Methods that score higher on ScanNet200 rely on either GT-trained proposals (*e.g.* Mask3D-based pipelines at up to 24.7 mAP, 16–554 s) or multi-view 2D streams with YOLO/SAM proposals (up to 26.0 mAP, ∼356 s). On ScanNet++, we achieve 22.9 mAP, surpassing the best prior method OpenTrack3D (20.6 mAP) which relies on multi-view 2D inputs and requires ∼320 seconds per scene (Tab. 4).

Our contributions are four-fold:

- SpaCeFormer-3M, the largest open-vocabulary 3D instance segmentation dataset (604K masks, 3.0M multi-view-consistent captions across 7.4K scenes), with 21× higher mask recall (54.3% vs 2.5% at IoU>0.5) than prior single-view pseudo-label pipelines.
- SpaCeFormer, a space-curve attention backbone combining sliding 3D window attention with Morton curve serialization for spatially coherent features.
- A RoPE-enhanced proposal-free decoder that predicts instance masks directly from learned queries without external heuristics.
- State-of-the-art results on ScanNet200 and ScanNet++ with strong zero-shot transfer across datasets.

2. Related Work

Closed-Vocabulary 3D Instance Segmentation. Classical methods assume a fixed label set for proposal generation and mask prediction. Mask3D (Schult et al., 2023) combines sparse convolutions with transformer-based mask refinement; ISBNet (Ngo et al., 2023) introduces box-aware dynamic convolutions for sharper masks. While effective on known categories, these methods rely on proposal networks trained on closed taxonomies, limiting generalization to novel classes.

Open-Vocabulary 3D Instance Segmentation. To generalize beyond fixed taxonomies, recent methods fuse 3D proposals with vision–language features from CLIP (Radford et al., 2021) or similar models. Nearly all adopt multi-stage pipelines: generate class-agnostic 3D masks, then classify via language alignment. OpenMask3D (Takmaz et al., 2023) aggregates multi-view CLIP features per proposal; Open3DIS (Nguyen et al., 2024) merges 2D and 3D proposals via hierarchical clustering; SAI3D (Yin et al., 2024) lifts 2D masks directly to 3D to bypass closed-vocabulary proposal networks; Open-YOLO 3D (Boudjoghra et al., 2025) aligns proposals with open-vocabulary 2D detectors. These pipelines depend on heavy 2D components (SAM (Kirillov et al., 2023), Grounded-SAM (Ren et al., 2024)) and repeated multi-view projections, incurring computational overhead and compounding errors across stages. A recent alternative, SOLE (Lee et al., 2025b), avoids explicit region proposals but still relies on ground-truth 3D mask supervision during training. We instead propose a proposal-free decoder that predicts masks directly from learned queries, trained entirely on pseudo-labels without any ground-truth 3D annotations.

Point Cloud Architectures. Open-vocabulary instance segmentation requires backbones that balance computational efficiency with spatial coherence for accurate mask prediction. Sparse convolutions (Choy et al., 2019; Thomas et al., 2019) and point transformers (Wu et al., 2022; 2024; Park et al., 2022) are widely used for 3D understanding. Point Transformer v3 (Wu et al., 2024) serializes point clouds via space-filling curves, *e.g.* Morton codes, for scalable attention, achieving strong results on semantic segmentation. However, Morton serialization scatters spatially adjacent points across attention windows, sacrificing the local coherence that instance segmentation requires for sharp boundaries. Our space-curve attention addresses this by combining spatial window attention, *i.e.* preserving local neighborhoods, with Morton serialization, *i.e.* providing attention diversity, yielding features suited for proposal-free instance prediction. We further adopt 3D rotary positional embeddings (RoPE) (Su et al., 2024), extending the 1D formulation from language models to encode 3D spatial relationships directly in attention.

Scalable 3D Annotation. Training open-vocabulary 3D models requires instance masks paired with language descriptions, yet such data is costly to annotate manually. Cap3D (Luo et al., 2023) aggregates multi-view captions for 3D assets; SceneVerse (Jia et al., 2024) scales vision–language data for indoor scenes; Mosaic3D (Lee et al., 2025a) aligns millions of 3D masks with text. However, 2D-to-3D lifting produces fragmented instances due to occlusion, and single-view captioning yields inconsistent descriptions across viewpoints. Multi-view mask clustering (Yan et al., 2024) addresses fragmentation; ranked view selection (Luo et al., 2024) improves caption consistency. We integrate both techniques to construct SpaCeFormer-3M, providing geometry-complete instances with view-consistent descriptions for open-vocabulary training.

3. Dataset Generation

Training open-vocabulary 3D models requires large-scale datasets pairing instance masks with language descriptions. Manual annotation at this scale is prohibitive, so recent work leverages 2D foundation models to automatically generate training data. However, prior pipelines (Yang et al., 2024b; Jiang et al., 2024; Lee et al., 2025a) suffer from two limitations: (1) fragmented 3D masks due to naive 2D-to-3D lifting, and (2) inconsistent captions from single-view prompting. We address both issues through a scalable pipeline that produces complete, geometry-consistent instances via multi-view mask clustering and view-consistent

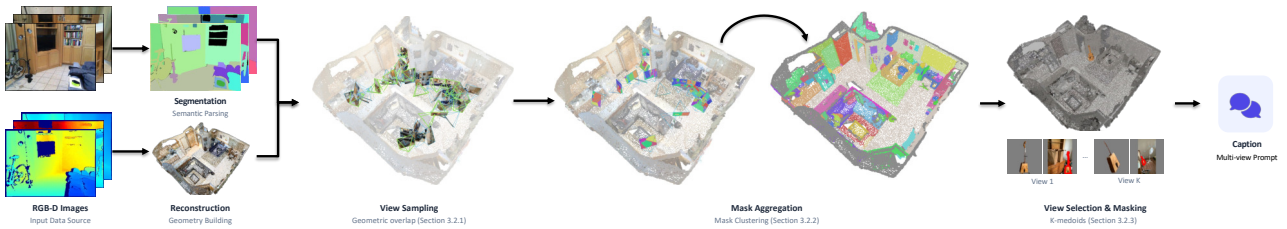

Figure 2. **Dataset Generation Pipeline.** Our pipeline generates high-quality 3D mask-caption pairs by (1) aggregating 2D masks into 3D instances through training-free multi-view clustering and (2) generating diverse, intrinsic-focused captions via structured multi-view VLM prompting. The process leverages large-scale RGB-D and video datasets to produce a massive corpus for open-vocabulary 3D learning.

descriptions via structured multi-view captioning (Figure 2).

3.1. Data Sources and Preprocessing

We aggregate four large-scale datasets spanning diverse capture conditions: ScanNet (Dai et al., 2017), ScanNet++ (Yeshwanth et al., 2023), Matterport3D (Chang et al., 2018), and ARKitScenes (Baruch et al., 2021). This combination covers professional high-quality scans (ScanNet++) and casual mobile captures (ARKitScenes), as well as diverse indoor environments (ScanNet, Matterport3D), ensuring the model generalizes across reconstruction qualities and scene types. All data are standardized into a unified format with calibrated intrinsics and poses (see Appendix A.6).

3.2. Annotation Pipeline

Step 1: Efficient View Sampling. Video datasets contain highly redundant frames that increase computation without improving coverage. We filter frames based on geometric overlap: iterating through frames sequentially, we select a frame only if its overlap with the most recently selected frame falls below a threshold. The overlap is computed as the intersection $\bigcap(\mathcal{P}_{t_i}, \mathcal{P}_{t_j})$ between backprojected point clouds, measuring the fraction of points in the current frame that have a nearest neighbor within a distance threshold in the reference frame. This greedy selection maximizes scene coverage while eliminating redundant viewpoints.

Step 2: Training-free 3D Mask Aggregation. Naive 2D-to-3D lifting produces fragmented masks because each view captures only partial object surfaces. We address this using MaskClustering (Yan et al., 2024): after detecting 2D masks with SAM2 (Ravi et al., 2024) and lifting them to 3D, we group segments based on spatial proximity, visibility, and containment. Strict filtering (visibility > 0.3, consensus > 0.9) removes incomplete fragments, yielding geometry-consistent instance masks. Crucially, this process also produces a one-to-many mapping between each aggregated 3D mask and its constituent 2D masks, which we leverage in Step 3 for multi-view captioning.

Step 3: Multi-view Captioning. Single-view captioning produces inconsistent descriptions because VLMs describe view-specific appearances rather than intrinsic object properties. We instead present multiple views to the VLM simultaneously: for each 3D instance, we use the one-to-many mapping from Step 2 to retrieve all views containing the instance, then select up to K representative views via k-medoids clustering on frame timestamps, weighted by mask visibility. These views are shown in two formats: (i) cropped with context and (ii) background-removed (Figure 3). A structured prompt (Appendix A.7) guides the VLM to describe intrinsic properties (shape, texture, material) and consistent spatial relationships. To enforce caption diversity, we sample multiple captions per instance by varying the view selection seed.

(a) *(b)* *(c)* *(d)*

Figure 3. **Multi-view Caption Prompt for LLM.** To generate high-fidelity captions, we select representative views of a 3D instance and provide them to a VLM in two formats: (a, c) cropped with spatial context and (b, d) background-removed masked views. See Appendix A.7.2 for details.

Figure 4 shows a qualitative example: a red leather armchair is accurately segmented in 3D and paired with multiple captions covering visual attributes, materials, and spatial context.

3.3. Dataset Statistics

SpaCeFormer-3M contains **604,127 3D instances** from **7,361 scenes**, paired with **3.0 million captions** (Table 1). This significantly exceeds prior datasets in scale, covering both professional scans (ScanNet++) and casual captures (ARKitScenes). Captions average 15.5 words, providing sufficient detail for open-vocabulary training.

Mask Quality Analysis. To validate our multi-view mask clustering, we compare against Mosaic3D's (Lee et al., 2025a) SAM2-based 2D-to-3D lifting on 312 ScanNet train scenes (Table 2). Mosaic3D produces only 16.1 masks per scene (vs. 32.0 GT instances), with 2.5% recall at IoU

(1) "The armchair features a smooth, red leather upholstery, providing a comfortable seating option."
(2) "A medium-sized, red armchair with a boxy shape sits adjacent to a round wooden table."
(3) "This red armchair offers a place to relax; its sturdy frame suggests durability and frequent use."
(4) "The armchair's design blends classic lines with a deep red hue, complementing the yellow wall."
(5) "Positioned near a table, the red armchair provides a functional and visually appealing seating area."

Figure 4. **Office/Lounge Scene Example.** A red leather armchair from an office waiting area, demonstrating the dataset's coverage of furniture in professional settings. Captions capture material properties (leather), spatial context (near table, yellow wall), and functional affordances (seating, relaxation).

> 0.5—the vast majority of objects are missed or fragmented. SpaCeFormer-3M generates 65.2 masks per scene with **54.3% recall** and **33.6% precision**, confirming that multi-view aggregation produces substantially more complete, geometry-consistent instances.

4. SpaCeFormer: Space-Curve Transformer

Design goal. SpaCeFormer, our Space-Curve Transformer, consists of a feature extraction backbone (Sec. 4–4.3) and a proposal-free decoder (Sec. 4.4). Our backbone is explicitly designed to serve the *proposal-free*, open-vocabulary instance decoder: it produces spatially coherent, instance-aligned voxel features and a CLIP-aligned feature map that the decoder consumes directly via mask attention. We strategically combine *spatial* window attention with *curve*-based (Morton code) serialization—windows preserve coherent local neighborhoods at fine resolutions, while curves introduce structured diversity in attention patterns.

4.1. Preliminaries

Let $\mathcal{P} = \{(p_i, f_i)\}_{i=1}^{M}$ be a point cloud where each point $p_i \in \mathbb{R}^3$ denotes a 3D coordinate and $f_i \in \mathbb{R}^{d_{in}}$ represents associated features (e.g., color). While our backbone processes data in a sparse voxel grid for efficiency, the overall pipeline preserves the point-based interface. We discretize the 3D space into a voxel grid $\mathcal{V} = \{v_1, \ldots, v_N\}$. For each non-empty voxel v_i, we compute a feature vector $\mathbf{x}_i \in \mathbb{R}^{d_{in}}$ by aggregating the features of its constituent points via average pooling. The input tensor is $\mathbf{X} \in \mathbb{R}^{N \times d_{in}}$.

Table 1. **Dataset statistics for SpaCeFormer-3M.** Our training corpus comprises 7,361 scenes with over 604K 3D instance masks and 3.0M captions aggregated from diverse indoor RGB-D datasets (ScanNet, ScanNet++, ARKitScenes, Matterport3D). Each mask is annotated with 5 captions from different viewpoints using our multi-view-aware captioning pipeline. "Avg masks/scene" indicates the average number of instance masks per scene, reflecting varying scene complexity across datasets.

Dataset	Scenes	Masks	Captions	Words	Avg masks/scene
ScanNet	1,201	79,320	396,600	6,105,677	66.04
ScanNet++	223	27,296	136,480	2,132,620	122.40
ARKitScenes	4,497	446,409	2,232,045	34,374,338	99.27
Matterport3D	1,440	51,102	255,510	3,958,785	35.49
Overall	**7,361**	**604,127**	**3,020,635**	**46,571,420**	**82.07**

Table 2. **3D Mask Quality vs. Ground Truth (312 ScanNet train scenes).** We compare auto-generated training masks against GT instance annotations. Mosaic3D (Lee et al., 2025a) uses SAM2 with naive 2D-to-3D lifting; Precision and recall are computed at IoU > 0.5.

Dataset	Masks / scene	Mean best-IoU	Prec. @0.5	Recall @0.5	IoU > 0.50
Mosaic3D (2025a)	16.1	0.247	4.8%	2.5%	3.8%
SpaCeFormer-3M (Ours)	**65.2**	**0.251**	**33.6%**	**54.3%**	**25.9%**

Terminology: Spatial Window vs. Attention Window Size. We distinguish two critical concepts:

- *Spatial window size*: The 3D geometric extent in voxel coordinates (e.g., $H \times W \times D$ voxels).
- *Attention window size*: The number of tokens (voxels) in an attention computation (sequence length L).

Space-Curve Attention Strategy. We combine two complementary attention mechanisms:

Spatial (Window) Attention: Voxels are partitioned into fixed *spatial windows* (fixed geometric extent). Due to 3D sparsity, each window contains a *variable number of voxels* (from 1 to $H \times W \times D$), yielding variable attention window sizes. This strictly preserves local geometric relationships.

Curve (Morton Code) Attention: Voxels are serialized via space-filling curves (Morton codes) $\pi : \{1, \ldots, N\} \to \{1, \ldots, N\}$ and partitioned into fixed-length segments (Wu et al., 2024). Each segment has a *fixed attention window size* (L voxels), but variable spatial extent. This introduces structured diversity in attention patterns.

Both mechanisms perform multi-head self-attention within each window, reducing complexity from $O(N^2)$ to $O(N \cdot L_{\text{max}})$, where L_{max} is the maximum attention window size. We employ full bidirectional attention within each window

(no causal masking). Fig. 5 illustrates the two approaches; details and analysis are in Sec. 4.3.

4.2. Architecture

The backbone f_θ follows a U-Net architecture with N_{blocks} transformer blocks (Fig. 7). The input voxel features are first embedded into a hidden dimension d: $\mathbf{H}^0 = \mathbf{X}\mathbf{W}_E$.

Convolution Block. Each transformer block incorporates local feature extraction through sparse 3D convolutions before the attention mechanism:

$$\mathbf{C}^l = \text{Conv3D}(\mathbf{H}^{l-1}) + \text{Conv}_{\text{shortcut}}(\mathbf{H}^{l-1}), \quad (1)$$

where Conv3D is a sparse 3D convolution processing local neighbors, and $\text{Conv}_{\text{shortcut}}$ is a residual connection. This design injects local geometric inductive biases into the network.

Transformer Block. Following the convolution, we apply windowed multi-head self-attention (MHSA) and a feed-forward network (FFN):

$$\mathbf{A}^l = \text{MHSA}(\text{LN}(\mathbf{C}^l)) + \mathbf{C}^l, \quad (2)$$

$$\mathbf{H}^l = \text{FFN}(\text{LN}(\mathbf{A}^l)) + \mathbf{A}^l, \quad (3)$$

where LN denotes layer normalization. The MHSA in Eq. (2) operates on the serialized windows defined in the preliminaries.

Encoder Path. We process features through N_{levels} encoder stages to capture multi-scale features. At each level ℓ:

$$\mathbf{E}^\ell = \text{TransformerBlocks}^\ell(\mathbf{E}^{\ell-1}), \quad (4)$$

$$\mathbf{E}^\ell_{\text{down}} = \text{DownConv}^\ell(\mathbf{E}^\ell), \quad (5)$$

where $\mathbf{E}^0 = \mathbf{H}^0$. We store $\mathbf{S}^\ell = \mathbf{E}^\ell$ for skip connections. DownConv^ℓ performs spatial downsampling (typically strided convolution).

Decoder Path. We progressively upsample and merge features. For each decoder level ℓ:

$$\mathbf{D}^\ell = \text{UpConv}^\ell(\mathbf{D}^{\ell+1}, \mathbf{S}^\ell), \quad (6)$$

$$\mathbf{D}^\ell_{\text{out}} = \text{TransformerBlocks}^\ell_{\text{dec}}(\mathbf{D}^\ell), \quad (7)$$

where UpConv^ℓ concatenates or adds the skip connection $\mathbf{S}^\ell$ to the upsampled features.

Order Shuffling. To prevent the model from overfitting to a specific serialization order, we randomly permute the serialization strategy similar to Wu et al. (2024). Additionally, for window attention, we randomly shift windows by half the window size ($W/2$) along various axes combinations (x, y, z, xy, xz, yz, xyz) to further increase robustness. See Appendix A.5.3 for details.

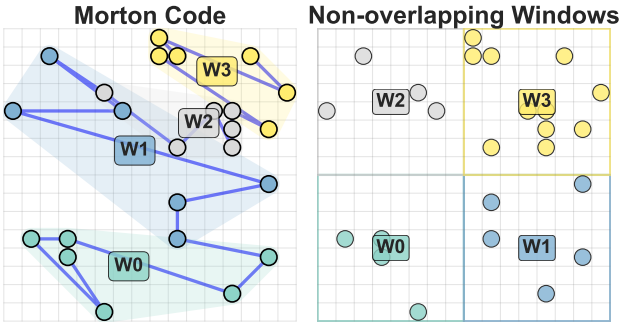

Figure 5. **Comparison of Attention Approaches.** (Left) Morton serialized attention showing the serialization path and resulting clusters. (Right) Non-overlapping window attention showing improved preservation of local geometric relationships. Quantitatively, our window-based approach reduces average within-window pairwise distance by 28.6% compared to Morton attention (visual coherence; see Sec. 4.3).

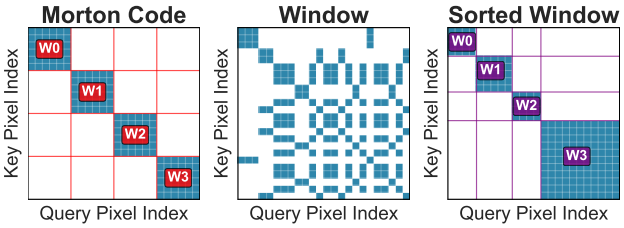

Figure 6. **Attention Pattern Comparison.** (Left) Morton code attention mask showing uniform block diagonal structure. (Middle) Window attention mask showing variable-sized blocks based on spatial proximity. (Right) Sorted window attention mask where pixels are reordered by window index to recover a block diagonal structure while preserving spatial relationships. Red, green, and purple lines indicate Morton, spatial, and sorted window boundaries, respectively.

Output Representation. The final voxel features $\mathbf{D}^1$ from Eq. (7) are mapped back to the original points $\mathcal{P}$ via nearest-neighbor interpolation (trilinear interpolation can also be used) to produce per-point features $\mathbf{F} \in \mathbb{R}^{M \times D}$. These features feed into the RoPE-enhanced instance decoder (Sec. 4.4). Additionally, we attach a lightweight projector to map features to a CLIP-aligned space $\mathbf{Z} \in \mathbb{R}^{N \times D_{\text{CLIP}}}$, enabling open-vocabulary applications.

4.3. Space-Curve Attention: Window + Morton Code

To directly support our proposal-free instance decoder, we require spatially coherent local neighborhoods that yield sharp, instance-aligned features. Our space-curve attention framework achieves this by strategically combining two complementary mechanisms.

The Space + Curve Combination. Existing methods (Wu et al., 2024) rely solely on Morton-ordered segments (MOS), which introduce beneficial randomness but sacrifice strict spatial locality. We strategically combine *spatial window*

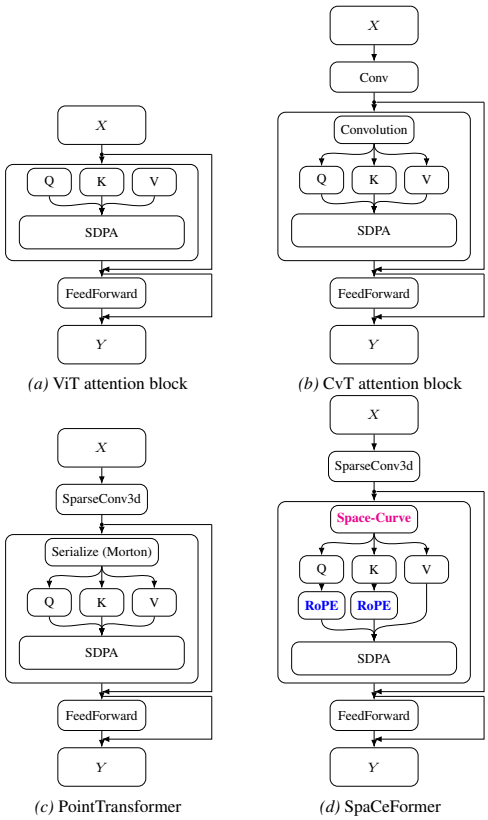

(a) ViT attention block *(b)* CvT attention block *(c)* PointTransformer *(d)* SpaCeFormer

Figure 7. **Attention block diagrams.** (Left to right) Attention blocks of ViT, CvT, PointTransformer, and our SpaCeFormer. Each shows vertical flow with residuals after MHSA and FeedForward. LayerNorm, DropPath, and projection shortcuts are omitted for clarity.

attention (Space) with *Morton code attention* (Curve). Spatial windows preserve coherent local geometry critical at high resolutions, while Morton curves provide structured diversity.

Key Distinction: Fixed Spatial Window vs. Fixed Attention Window Size. Morton-based methods partition serialized voxels into fixed-length segments (fixed attention window size L), arbitrarily splitting spatially proximate voxels. Our spatial windows instead use fixed **spatial extents**, containing a variable number of voxels, strictly preserving local spatial relationships.

To quantify the spatial coherence improvement, we measure the average pairwise distance between voxels within the same attention window (see Appendix A.5.1 for metric definition). Fig. 6 shows that spatial window attention achieves a 28.6% reduction in average spatial distance compared to Morton-based attention, significantly better preserving local geometric relationships. For implementation details and pseudocode, see Appendix A.5.2 and A.5.4.

3D Rotary Positional Embedding (RoPE). To encode 3D spatial relationships in our proposal-free architecture, we employ 3D rotary positional embeddings (RoPE) that directly encode position information into the attention mechanism through rotation transformations. For voxels at positions $\mathbf{p}_i = (x_i, y_i, z_i)$ and $\mathbf{p}_j = (x_j, y_j, z_j)$, the attention is computed as:

$$\langle \mathbf{q}_i, \mathbf{k}_j \rangle = \mathbf{q}_i \mathbf{R}_{\Theta, \mathbf{p}_j - \mathbf{p}_i} \mathbf{k}_j^\top, \tag{8}$$

where $\mathbf{R}_{\Theta,\Delta\mathbf{p}}$ is a block-diagonal rotation matrix parameterized by relative position $\Delta\mathbf{p} = (x_j - x_i, y_j - y_i, z_j - z_i)$:

$$\mathbf{R}_{\Theta,\Delta\mathbf{p}} = \begin{bmatrix} \mathbf{R}_x(\theta_x) & & \\ & \mathbf{R}_y(\theta_y) & \\ & & \mathbf{R}_z(\theta_z) \end{bmatrix}, \tag{9}$$

where each $\mathbf{R}_d(\theta_d)$ for $d \in \{x, y, z\}$ is a 2D rotation matrix applied to pairs of feature dimensions, and $\theta_d = \Delta p_d / \text{base}^{2m/d_h}$ for frequency index m. The block-diagonal structure allows independent encoding of each spatial dimension. We provide detailed formulations in Appendix A.1.

In our backbone, RoPE is applied with *relative* displacements within local sliding windows (Sec. 4.3); in the instance decoder (Sec. 4.4), RoPE is applied for query–scene cross-attention to preserve point locations.

4.4. Proposal-Free Instance Segmentation Decoder

Building upon our SpaCeFormer-backbone (Sec. 4), we present a *proposal-free*, open-vocabulary instance segmentation decoder. Unlike multi-stage pipelines that rely on external region proposal networks (*e.g.* Mask3D (Schult et al., 2023), Segment3D (Huang et al., 2024a)) followed by per-proposal feature extraction and heuristic merging, we predict masks directly from a fixed set of learned queries via mask attention (Cheng et al., 2022), analogous to DETR (Carion et al., 2020). We term this *proposal-free* because the decoder requires no external modules—queries are learned end-to-end and decoded in a single forward pass without multi-stage processing.

Architecture. Our decoder (Fig. 8) consumes per-point features $\mathbf{F} \in \mathbb{R}^{N \times D}$ obtained by gathering the backbone's features (Sec. 4) from voxels to points. We initialize Q learned query embeddings $\mathbf{Q}^{(0)} \in \mathbb{R}^{Q \times D}$ typically with $Q = 200$.

Iterative Refinement with RoPE. The decoder refines queries through T iterations (typically $T = 3$) of cross-attention, self-attention, and FFN. We randomly sample S points once per forward pass for efficiency. In cross-attention, we apply 3D Rotary Position Embeddings (RoPE, Eq. (8)) to keys based on their 3D coordinates. Since we use learned queries which do not go through RoPE, the rotated keys encode their absolute coordinates, which we find critical for performance (Tab. 8). Parameters are shared across iterations.

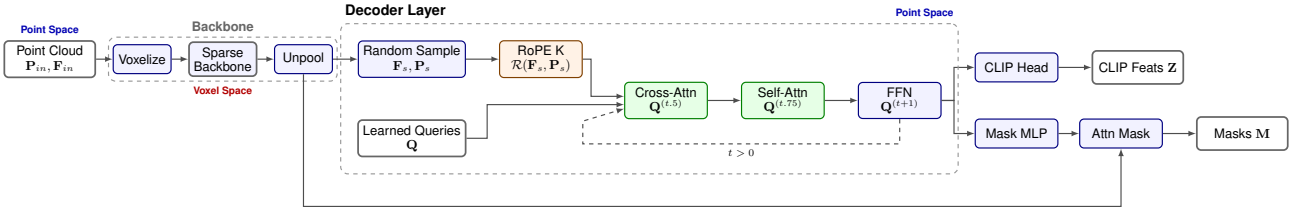

Figure 8. **RoPE-Enhanced Instance Segmentation Decoder Architecture.** The decoder iteratively refines query tokens through cross-attention with scene features and self-attention among queries. RoPE is applied separately to encode 3D spatial relationships in both attention mechanisms using absolute coordinates from the scene.

Prediction Heads. After T iterations, we discard samples and use all points without sampling. We predict instance masks via dot-product between final queries and point features: $\mathbf{M} = \sigma(\mathbf{F}(\mathbf{W}_M \mathbf{Q}^{(T)})^\top) \in \mathbb{R}^{N \times Q}$, where each column represents per-point soft assignment to an instance. We also predict foreground/background logits $\mathbf{C} = \mathbf{W}_C \mathbf{Q}^{(T)} \in \mathbb{R}^{Q \times 2}$, and CLIP features $\mathbf{Z} = \mathbf{W}_{\text{CLIP}} \mathbf{Q}^{(T)} \in \mathbb{R}^{Q \times D_{\text{CLIP}}}$.

Open-Vocabulary Inference. At inference, we use the predicted CLIP embeddings $\mathbf{Z}$ for each instance. For evaluation, we assign labels by taking the argmax of the cosine similarity between $\mathbf{Z}$ and the text embeddings of all possible labels.

Optimization. We train with a composite objective $\mathcal{L} = \lambda_{\text{mask}} \mathcal{L}_{\text{mask}} + \lambda_{\text{CLIP}} \mathcal{L}_{\text{CLIP}} + \lambda_{\text{fg}} \mathcal{L}_{\text{fg}}$, where ground-truth assignment uses Hungarian matching. The loss combines mask loss (Cheng et al., 2022) (BCE + Dice), CLIP loss (Oord et al., 2018) (InfoNCE), and foregroundness loss for query objectness. We optimize the network with Muon (Jordan et al., 2024) for all hidden-layer parameters that are at least two-dimensional, and AdamW for non-matrix parameters. See Appendix A.9 for details.

5. Experiments

Datasets. Following the data generation pipeline described in Sec. 3, we construct our training corpus from large-scale RGB-D and multi-view datasets. Our data sources include standard indoor RGB-D datasets (Dai et al., 2017; Yeshwanth et al., 2023; Chang et al., 2018; Baruch et al., 2021). Each scene is processed through our annotation pipeline to generate high-quality 3D mask-caption pairs, combining training-free multi-view mask aggregation with multi-view-aware caption generation; this yields 54.3% mask recall at IoU>0.5 compared to 2.5% for prior single-view pipelines (Table 2). We evaluate on three benchmarks: Replica (Straub et al., 2019) (8 scenes, zero-shot), ScanNet++ (Yeshwanth et al., 2023) (100 classes), and ScanNet200 (Rozenberszki et al., 2022) (200 classes).

Implementation Details. We train on 4 nodes × 8 NVIDIA H100 GPUs (80GB each) with batch size 32 for 25k iterations (∼1.5 days) using Muon (Jordan et al., 2024) and AdamW. Inference is performed on a single NVIDIA H100 GPU; the reported 0.14s per scene is the end-to-end total for voxelization + backbone forward + proposal-free decoder + mask extraction, and excludes one-time CLIP text encoding (∼0.02s, amortized across scenes). We primarily evaluate open-vocabulary 3D *instance* segmentation, and report semantic segmentation as an auxiliary task.

5.1. Comparison with Existing Methods

Zero-Shot Evaluation on Replica. We first evaluate on Replica (Straub et al., 2019), a synthetic indoor dataset with 8 scenes—crucially, never seen during training—to assess cross-domain generalization. Table 3 shows that SpaCeFormer achieves 24.1 mAP, setting a new state of the art while surpassing Open-YOLO 3D (Boudjoghra et al., 2025) (23.7 mAP) and OpenTrack3D (Zhou et al., 2025) (23.9 mAP). Our method is **119× faster** than Open-YOLO 3D (0.14s vs. 16.6s per scene) and **3,900× faster** than OpenMask3D (547.3s per scene), while using only 3D input. All baselines require 3D+2D inputs with external region proposal networks and sequential per-frame 2D processing, whereas SpaCeFormer processes the entire 3D scene in a single forward pass.

Cross-Dataset Evaluation on ScanNet++. We evaluate on ScanNet++ (Yeshwanth et al., 2023), which features 100 fine-grained semantic classes and higher-quality reconstructions. Table 4 shows that SpaCeFormer achieves 22.9 mAP, surpassing the prior state-of-the-art OpenTrack3D (20.6 mAP) which relies on multi-view 2D inputs and YOLO-World + SAM2 proposals. While all baselines require multi-stage 3D+2D pipelines taking minutes per scene (e.g., MaskClustering at 600s, OpenMask3D at ∼554s), our proposal-free method achieves the best mAP with only 0.14s per scene—**over 4,000× faster**. These results demonstrate strong generalization across datasets with different reconstruction qualities and class taxonomies.

Evaluation on ScanNet200. Table 5 presents a comprehensive comparison on ScanNet200 (200 classes), categorized by input type and region proposal network. Most prior work relies on closed-vocabulary 3D region propos-

Table 3. **Zero-shot 3D instance segmentation on Replica (Straub et al., 2019) (8 scenes).** All methods evaluated zero-shot (Replica is not used for training). We categorize by region proposal type: **(a)** GT-trained 3D proposals (Mask3D (Schult et al., 2023) or ISBNet (Ngo et al., 2023)). **(b)** Open-vocabulary proposals (no GT 3D annotations). **(c)** Proposal-free methods (with and without ground-truth 3D mask supervision). Baseline numbers from Open-YOLO 3D (Boudjoghra et al., 2025) and OpenTrack3D (Zhou et al., 2025).

	Method	Inputs	Region Proposal Network			mAP	mAP_{50}	mAP_{25}	Latency	Speedup
			Name	No GT	Open vocab					
(a)	OpenScene-3D (2023)	3D	Mask3D (2023)	✗	✗	8.2	10.5	12.6	4.3s	31×
	OpenScene-2D (2023)	3D + 2D	Mask3D (2023)	✗	✗	10.9	15.6	17.3	317.3s	2267×
	OpenMask3D (2023)	3D + 2D	Mask3D (2023)	✗	✗	13.1	18.4	24.2	547.3s	3909×
	Open3DIS (2024)	3D + 2D	ISBNet (2023) + SAM	✗	✗	18.5	24.5	28.2	188.0s	1343×
	Open3DIS (3D prop. only) (2024)	3D	ISBNet (2023)	✗	✗	14.9	18.8	23.6	35.1s	251×
	Open-YOLO 3D (2025)	3D + 2D	Mask3D (2023)	✗	✗	23.7	28.6	34.8	16.6s	119×
	Details Matter (2D) (2025)	2D	Mask3D + GSAM	✗	✗	20.8	32.4	38.5	–	–
	Details Matter (3D) (2025)	3D	Mask3D + GSAM	✗	✗	22.0	26.7	32.5	–	–
	Details Matter (2025)	3D + 2D	Mask3D + GSAM	✗	✗	22.6	31.7	37.7	597s	4264×
(b)	OVIR-3D (2023)	3D + 2D	Detic (2022)	✓	✓	11.1	20.5	27.5	52.7s	376×
	OV-MAP (2024)	3D + 2D	SAM (2023)	✓	✓	14.2	19.6	28.1	–	–
	PoVo (2024)	3D + 2D	SAM (2023)	✓	✓	20.8	28.7	34.4	–	–
	BoxOVIS (2025)	3D + 2D	Box detector + SAM	✓	✓	24.0	31.8	37.4	43.7s	312×
	OpenTrack3D (2025)	3D + 2D	YOLO-World + SAM2	✓	✓	23.9	36.4	47.6	∼62s	443×
(c)	SOLE (2025b)	3D only	Not required (proposal-free)	✗	✓	24.7	31.8	40.3	–	–
	SpaCeFormer (Ours)	3D only	Not required (proposal-free)	✓	✓	**24.1**	**31.8**	**37.1**	**0.14s**	—

Table 4. **Zero-shot 3D instance segmentation on ScanNet++ (100 classes).** We compare open-vocabulary methods that assign semantic labels from text queries. All methods use the ScanNet++ validation set. * uses closed-vocabulary Mask3D proposals trained with ground-truth annotations.

	Method	Inputs	Region Proposal Network			mAP	mAP_{50}	mAP_{25}	Latency	Speedup
			Name	No GT	Open vocab					
(a)	OpenMask3D (2023)	3D + 2D	Mask3D (2023)	✗	✗	2.0	2.7	3.4	∼554s†	3957×
	OVIR-3D (2023)	3D + 2D	Mask3D (2023)	✗	✗	3.6	5.7	7.3	–	–
(b)	MaskClustering (2024)	3D + 2D	CropFormer (2023)	✓	✓	7.8	10.7	12.1	600s	4286×
	Segment3D (2024a)	3D + 2D	SAM (2023)	✓	✓	10.1	17.7	20.2	–	–
	Open3DIS (2024)	3D + 2D	SAM-HQ (2023)	✓	✓	11.9	18.1	21.7	∼360s†	2571×
	Any3DIS (2025)	3D + 2D	SAM2 (2024)	✓	✓	12.9	19.0	21.9	∼36s†	257×
	OpenSplat3D (2025)	3D + 2D	SAM + GS	✓	✓	16.5	29.7	39.0	–	–
	OpenTrack3D (2025)	3D + 2D	YOLO-World + SAM2	✓	✓	20.6	34.2	43.4	∼320s†	2286×
(c)	SpaCeFormer (Ours)	3D only	Not required (proposal-free)	✓	✓	**22.9**	**33.7**	**41.6**	**0.14s**	—

als from Mask3D (Schult et al., 2023), which requires ground-truth annotations for training. When methods switch to open-vocabulary proposals from Segment3D (Huang et al., 2024a), performance drops dramatically (Mosaic3D: 11.8→2.7 mAP). Our proposal-free architecture eliminates this dependence entirely. SpaCeFormer achieves 11.1 mAP without any proposals, outperforming all open-vocabulary methods by a large margin (4.1× better than Mosaic3D with Segment3D proposals), while requiring only 0.14 seconds per scene. For reference, fully supervised closed-vocabulary methods achieve 27.4 mAP (Mask3D) and 30.6 mAP (OneFormer3D) with GT labels. Qualitative results in Fig. 9 demonstrate accurate segmentation across diverse object categories, and Figure 10 further shows successful generalization to novel categories (*e.g.*, Snoopy, X-mas) absent from the ScanNet200 taxonomy on Matterport3D test scenes. For detailed per-class performance breakdown and confusion analysis, see Appendix A.14.

Class-Agnostic Mask Quality. Table 6 evaluates mask quality independent of semantic labeling. Despite using only 3D point clouds, SpaCeFormer achieves 22.5 AP, outperforming multi-stage 3D+2D methods like MaskClustering (19.2 AP) and OnlineAnySeg (18.6 AP). More notably, our AP_{50} (45.7) and AP_{25} (64.4) substantially exceed all open-vocabulary baselines, including Any3DIS 2D-only (45.2 / 55.0), demonstrating that our proposal-free decoder produces high-quality masks with tight boundaries.

5.2. Ablation Study

Space-Curve Attention. We validate our space-curve attention design by comparing three variants: Morton-curve ordering only (PTv3 baseline), window attention only, and their strategic combination. Table 7 demonstrates that the combination of window and Morton-curve attention (our space-curve attention) achieves the best performance, validating our architectural choice to combine these comple-

Table 5. **Zero-shot 3D instance segmentation on ScanNet200 (Rozenberszki et al., 2022).** For a fair comparison, we categorize methods by input types and region proposal network: **(a)** Methods using both 3D point cloud and 2D RGB-D images, with 3D+2D region proposals and 2D CLIP inference. **(b)** Methods using both 3D+2D inputs, with region proposals from Mask3D (Schult et al., 2023) (closed-vocab) and 2D CLIP inference. **(c)** Methods using only 3D input with Mask3D (Schult et al., 2023). **(d)** Methods using only 3D input with open-vocabulary 3D region proposals. † denotes results without test-time voting, following the official implementation. Latency reports end-to-end runtime (seconds) per scene on ScanNet validation, including both proposal generation and method inference. EmbodiedSAM (Xu et al., 2025) and OnlineAnySeg (Tang et al., 2025) are omitted as they report only class-agnostic (not semantic) instance segmentation on ScanNet200.

	Method	Inputs	Region Proposal Network			mAP	mAP_{50}	mAP_{25}	mAP_{head}	$mAP_{com.}$	mAP_{tail}	Latency
			Name	No GT	Open vocab							
(a)	Open3DIS (2024)	3D + 2D	Superpoints (2004) + ISBNet (2023) + Grounded-SAM (2024)	✗	✗	23.7	29.4	32.8	27.8	21.2	21.8	33.5
	Any3DIS (2025)	3D + 2D	ISBNet (2023) + SAM2 (2024)	✗	✗	25.8	–	–	27.4	23.8	26.4	–
	Details Matter (2025)	3D + 2D	Mask3D (2023) + GSAM (2024)	✗	✗	25.8	32.5	36.2	26.3	23.2	28.2	–
	SAI3D (2024)	3D + 2D	Superpoints (2004) + SAM (2023)	✓	✓	12.7	18.8	24.1	12.1	10.4	16.2	75.2
	MaskClustering (2024)	3D + 2D	CropFormer (2023)	✓	✓	12.0	23.3	30.1	–	–	–	–
	SAM2Object (2025)	3D + 2D	SAM2 (2024)	✓	✓	13.3	19.0	23.8	–	–	–	–
	OpenTrack3D (2025)	3D + 2D	YOLO-World + SAM2 (2024)	✓	✓	26.0	37.7	45.4	–	–	–	∼356
(b)	OpenScene-2D (2023)	3D + 2D	Mask3D (2023)	✗	✗	11.7	15.2	17.8	13.4	11.6	9.9	-
	OpenScene-2D/3D (2023)	3D + 2D	Mask3D (2023)	✗	✗	5.3	6.7	8.1	11.0	3.2	1.1	-
	OpenMask3D (2023)	3D + 2D	Mask3D (2023)	✗	✗	15.4	19.9	23.1	17.1	14.1	14.9	553.9
	Open-YOLO 3D (2025)	3D + 2D	Mask3D (2023)	✗	✗	24.7	31.7	36.2	27.8	24.3	21.6	21.8
(c)	OpenScene-3D (2023)	3D	Mask3D (2023)	✗	✗	4.8	6.2	7.2	10.6	2.6	0.7	1.1
	RegionPLC (2024b)	3D	Mask3D (2023)	✗	✗	6.3	8.6	9.7	15.6	1.0	1.7	1.0
	OpenIns3D (2024b)	3D	Mask3D (2023)	✗	✗	8.8	10.3	14.4	16.0	6.5	4.2	285.2
	OpenIns3D† (2024b)	3D	Mask3D (2023)	✗	✗	3.3	5.0	5.6	7.0	1.4	1.2	50.0
	Mosaic3D (2025a)	3D	Mask3D (2023)	✗	✗	11.8	16.0	17.8	21.8	7.2	5.4	1.0
	SpaCeFormer w/ Proposal	3D	Mask3D (2023)	✗	✗	16.7	21.9	24.8	22.8	16.4	9.9	1.1
(d)	OpenScene-3D (2023)	3D	Segment3D (2024a)	✓	✓	0.6	1.0	1.6	1.4	0.4	0.0	2.0
	RegionPLC (2024b)	3D	Segment3D (2024a)	✓	✓	1.5	2.1	2.6	2.3	0.2	1.9	1.9
	OpenIns3D† (2024b)	3D	Segment3D (2024a)	✓	✓	1.7	2.7	3.7	3.2	0.8	1.0	64.8
	Mosaic3D (2025a)	3D	Segment3D (2024a)	✓	✓	2.7	4.2	5.7	3.8	2.0	2.4	1.9
	Mosaic3D w/ Decoder	3D	Not required (proposal-free)	✓	✓	3.9	7.0	12.3	6.6	2.1	2.8	1.2
	SpaCeFormer	3D	Not required (proposal-free)	✓	✓	**11.1**	**18.8**	**24.3**	**13.2**	**9.5**	**10.6**	**0.14**

Table 6. **Class-agnostic 3D instance segmentation on ScanNet200.** We report mask-quality metrics (AP, AP_{50}, AP_{25}) without semantic labels, evaluated on ScanNet200 validation (198 foreground classes). Methods are grouped by input modality. Latency is end-to-end seconds per scene. * uses closed-vocabulary ISBNet proposals trained with ground-truth annotations. † online methods that report per-frame FPS (15 and 10, respectively) rather than per-scene latency.

Method	Inputs	AP	AP_{50}	AP_{25}	Latency
3D + 2D methods (use multi-view RGB-D at inference)					
OVIR-3D (2023)	3D + 2D	14.4	27.5	38.8	466.8
OnlineAnySeg† (2025)	3D + 2D	18.6	36.1	53.5	–
MaskClustering (2024)	3D + 2D	19.2	36.6	51.7	156.0
EmbodiedSAM† (2025)	3D + 2D	**42.2**	–	–	–
Any3DIS* (2025)	3D + 2D	**42.5**	**51.2**	**54.5**	∼36
2D-only methods					
Any3DIS (2025)	2D	**32.5**	**45.2**	**55.0**	∼36
3D-only methods (point cloud only at inference)					
SpaCeFormer (Ours)	3D	**22.5**	**45.7**	**64.4**	**0.2**

Table 7. **Space-Curve Attention Ablation.** Comparing window attention only, Morton-curve ordering only, and their strategic combination. Evaluated on ScanNet200 zero-shot instance segmentation validation set.

			Class Agnostic			200-Way Class Specific		
Name	Window	Morton	AP	AP25	AP50	mAP	mAP25	mAP50
SpaCeFormer	✓	–	**0.25466**	0.68991	0.49903	0.09517	0.22476	0.16815
SpaCeFormer	–	✓	0.23311	0.67391	0.47290	0.09470	0.22315	0.16410
SpaCeFormer	✓	✓	0.25178	**0.69114**	**0.50447**	**0.11092**	**0.24312**	**0.18783**

Table 8. Ablation of positional encoding (PE) strategy for zero-shot 3D instance segmentation on ScanNet200 (validation). We tested absolute positional embedding (APE); learnable relative positional bias (Bias); rotary positional embedding (RoPE); and no positional encoding (No PE). We train for 25k iterations with Muon (lr 2e−3) using batch size 2 on 32 GPUs.

Method	mAP	mAP_{50}	mAP_{25}	mAP_{head}	$mAP_{com.}$	mAP_{tail}
SpaCeFormer (No PE)	5.97	11.47	17.27	9.68	4.50	3.43
SpaCeFormer (APE)	5.95	11.54	16.10	9.35	5.37	2.68
SpaCeFormer (Bias)	6.46	11.82	17.22	9.20	5.15	4.84
SpaCeFormer (RoPE)	**7.60**	**13.73**	**18.57**	**10.62**	**6.47**	**5.42**

mentary mechanisms.

Positional Encoding Strategy. Table 8 compares different positional encoding strategies for the decoder. **RoPE achieves 7.60 mAP**, outperforming alternatives including no positional encoding (5.97 mAP), absolute positional encoding (5.95 mAP), and positional bias (6.46 mAP). This validates our choice to encode 3D geometry directly within attention through rotary positional embeddings.

Query Initialization Strategy. We compare different query initialization strategies for the decoder: learned queries (following DETR), Farthest Point Sampling (FPS), and random sampling. Table 9 shows that learned query initialization

Table 9. Ablation of open-vocabulary 3D instance segmentation training and query initialization strategy for zero-shot 3D instance segmentation on ScanNet200 (validation). We compare 100 learned queries, Farthest Point Sampling (FPS), and random initialization. We train for 25k iterations. AP, AP_{25}, AP_{50} are the class agnostic average precision. The other metrics are the class-wise mean average precision.

	Class Agnostic			200-Way Class Specific		
Name	**AP**	**AP25**	**AP50**	**mAP**	**mAP25**	**mAP50**
SpaCeFormer (Learned)	**0.19819**	**0.62469**	**0.41561**	0.06443	**0.18213**	0.12037
SpaCeFormer (FPS)	0.17970	0.58387	0.38380	**0.07164**	0.17942	**0.13114**
SpaCeFormer (Random)	0.14635	0.52839	0.32332	0.05634	0.14893	0.10230

achieves the best performance (19.82 AP class-agnostic), outperforming FPS (17.97 AP) and random initialization (14.64 AP). This motivated our choice of learned query initialization in the final model.

Hyperparameter Choices. We use random key sampling (with a training-only cap) for the decoder's cross-attention, default normalization, and window attention at the finest hierarchical levels (window sizes 64 and 48 for the highest and second-highest resolution layers). Full ablations on key sampling strategies, normalization placement, and window size configurations are provided in Appendix A.11.

Figure 9. **Qualitative Results on ScanNet200.** We visualize the 3D masks predicted by our model. The results demonstrate the ability to segment a wide range of objects, including furniture like sofa chairs, mini fridges, monitors, and office chairs.

Backbone Comparison. We compare our Space-Curve Transformer backbone against PTv3 under identical training conditions. Space-Curve Transformer consistently outperforms PTv3 across all four benchmarks (e.g., 16.55 vs. 14.77 mIoU on ScanNet200), validating that spatial window attention provides meaningful gains beyond Morton-curve serialization alone. Full configuration analysis in Appendix A.12.

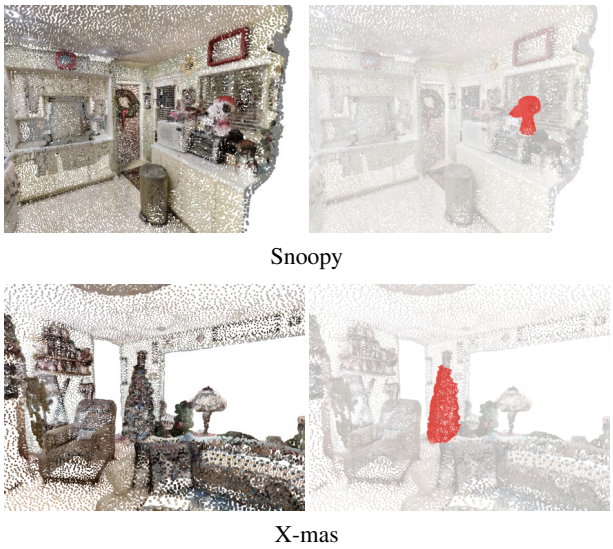

Figure 10. **Novel Category Segmentation on Matterport3D.** We visualize predictions on categories absent from the ScanNet200 taxonomy. Left: input point cloud. Right: predicted mask (red). The results demonstrate that our model generalizes to novel objects unseen during training, such as a toy and a Christmas tree.

6. Conclusion

We introduced SpaCeFormer, a proposal-free approach to open-vocabulary 3D instance segmentation that addresses key limitations in both data quality and model architecture. Our contributions center on two components: (1) SpaCeFormer-3M, a large-scale dataset with 3.0M multi-view-consistent captions over 604K geometry-consistent instances generated via training-free multi-view mask clustering and view-consistent captioning, and (2) space-curve attention that combines spatial window attention with Morton curve serialization to preserve local geometric relationships while maintaining efficiency. These spatially coherent features enable our RoPE-enhanced decoder to predict instance masks from learned queries, where absolute 3D positional encoding allows geometry-aware reasoning about spatial proximity and object categories. SpaCeFormer operates at **0.14 seconds per scene**, interactive rates that are 2–3 orders of magnitude faster than multi-stage 2D+3D pipelines, while reaching **24.1 zero-shot mAP on Replica** (Fig. 1, Pareto-optimal among open-vocabulary methods that do not use GT 3D supervision), 22.9 mAP on ScanNet++ (surpassing all prior methods, including those with multi-view 2D inputs), and 11.1 mAP on ScanNet200 under its matched setting (proposal-free, 3D-only, no GT 3D annotations).

Limitations. A gap remains between our 3D-only proposal-

free setup and methods that use either multi-view 2D inputs or GT-trained proposals on ScanNet200 (*e.g.* OpenTrack3D at 26.0 mAP with 2D+3D inputs, Open-YOLO 3D at 24.7 mAP with Mask3D proposals). Our evaluation focuses on indoor scenes; generalization to outdoor or in-the-wild environments remains to be validated. The fixed number of learned queries (Q=200) may also limit performance on scenes with many small objects.

References

Baruch, G., Chen, Z., Dehghan, A., Feigin, Y., Fu, P., Gebauer, T., Kurz, D., Dimry, T., Joffe, B., Schwartz, A., et al. Arkitscenes: A diverse real-world dataset for 3d indoor scene understanding using mobile rgb-d data. In *Thirty-fifth Conference on Neural Information Processing Systems Datasets and Benchmarks Track (Round 1)*, 2021.

Boudjoghra, M. E. A., Dai, A., Lahoud, J., Cholakkal, H., Anwer, R. M., Khan, S., and Khan, F. S. Open-YOLO 3d: Towards fast and accurate open-vocabulary 3d instance segmentation. In *The Thirteenth International Conference on Learning Representations*, 2025.

Carion, N., Massa, F., Synnaeve, G., Usunier, N., Kirillov, A., and Zagoruyko, S. End-to-end object detection with transformers. In *European Conference on Computer Vision*, pp. 213–229. Springer, 2020.

Chang, A., Dai, A., Funkhouser, T., Halber, M., Niebner, M., Savva, M., Song, S., Zeng, A., and Zhang, Y. Matterport3d: Learning from rgb-d data in indoor environments. In *7th IEEE International Conference on 3D Vision, 3DV 2017*, pp. 667–676. Institute of Electrical and Electronics Engineers Inc., 2018.

Chen, Y., Guo, X., Chen, W., and Wang, Y. Details matter: Accurate 3d open-vocabulary instance segmentation. *arXiv preprint arXiv:2507.23134*, 2025.

Cheng, B., Misra, I., Schwing, A. G., Kirillov, A., and Girdhar, R. Masked-attention mask transformer for universal image segmentation. In *CVPR*, pp. 1290–1299, 2022.

Choy, C., Gwak, J., and Savarese, S. 4d spatio-temporal convnets: Minkowski convolutional neural networks. In *Proceedings of the IEEE/CVF conference on computer vision and pattern recognition*, pp. 3075–3084, 2019.

Dai, A., Chang, A. X., Savva, M., Halber, M., Funkhouser, T., and Nießner, M. Scannet: Richly-annotated 3d reconstructions of indoor scenes. In *Proceedings of the IEEE conference on computer vision and pattern recognition*, pp. 5828–5839, 2017.

Driess, D., Xia, F., Sajjadi, M. S., Lynch, C., Chowdhery, A., Ichter, B., Wahid, A., Tompson, J., Vuong, Q., Yu, T., et al. Palm-e: An embodied multimodal language model. In *International Conference on Machine Learning*, pp. 8469–8488. PMLR, 2023.

Felzenszwalb, P. F. and Huttenlocher, D. P. Efficient graph-based image segmentation. *International journal of computer vision*, 59:167–181, 2004.

Guo, J., Ma, X., Fan, Y., Liu, H., and Li, Q. Semantic gaussians: Open-vocabulary scene understanding with 3d gaussian splatting. In *European Conference on Computer Vision*, 2024.

Huang, R., Peng, S., Takmaz, A., Tombari, F., Pollefeys, M., Song, S., Huang, G., and Engelmann, F. Segment3d: Learning fine-grained class-agnostic 3d segmentation without manual labels. In *European Conference on Computer Vision*, 2024a.

Huang, Z., Wu, X., Chen, X., Zhao, H., Zhu, L., and Lasenby, J. Openins3d: Snap and lookup for 3d open-vocabulary instance segmentation. In *European Conference on Computer Vision*, 2024b.

Jia, B., Chen, Y., Yu, H., Wang, Y., Niu, X., Liu, T., Li, Q., and Huang, S. Sceneverse: Scaling 3d vision-language learning for grounded scene understanding. In *European Conference on Computer Vision*, pp. 289–310. Springer, 2024.

Jia, H. et al. Sam2object: Zero-shot 3d object segmentation via sam2. In *CVPR*, 2025.

Jiang, L., Shi, S., and Schiele, B. Open-vocabulary 3d semantic segmentation with foundation models. In *CVPR*, pp. 21284–21294, 2024.

Jordan, K., Jin, Y., Boza, V., You, J., Cesista, F., Newhouse, L., and Bernstein, J. Muon: An optimizer for hidden layers in neural networks, 2024. URL https://kellerjordan.github.io/posts/muon/.

Ke, L., Ye, M., Danelljan, M., Liu, Y., Tai, Y.-W., Tang, C.-K., and Yu, F. Segment anything in high quality. In *NeurIPS*, 2023.

Kim, J., Park, Y., Yoon, H.-J., and Zhang, B.-T. OV-MAP: Open-vocabulary zero-shot 3d instance segmentation map for robots. In *IEEE/RSJ International Conference on Intelligent Robots and Systems (IROS)*, 2024.

Kirillov, A., Mintun, E., Ravi, N., Mao, H., Rolland, C., Gustafson, L., Xiao, T., Whitehead, S., Berg, A. C., Lo, W.-Y., et al. Segment anything. In *Proceedings of the IEEE/CVF International Conference on Computer Vision*, pp. 4015–4026, 2023.

Koch, S., Navarro, M., Avetisyan, A., and Dai, A. Opensplat3d: Open-vocabulary 3d instance segmentation with gaussian splatting. *arXiv preprint arXiv:2503.07768*, 2025.

Lee, J., Park, C., Choe, J., Wang, Y.-C. F., Kautz, J., Cho, M., and Choy, C. Mosaic3d: Foundation dataset and model for open-vocabulary 3d segmentation. In *Proceedings of the Computer Vision and Pattern Recognition Conference*, pp. 14089–14101, 2025a.

Lee, S., Zhao, Y., and Lee, G. H. Segment any 3d object with language. In *International Conference on Learning Representations (ICLR)*, 2025b.

Liu, Z., Miao, Z., Zhan, X., Wang, J., Gong, B., and Yu, S. X. Large-scale long-tailed recognition in an open world. In *Proceedings of the IEEE/CVF conference on computer vision and pattern recognition*, pp. 2537–2546, 2019.

Liu, Z., Lin, Y., Cao, Y., Hu, H., Wei, Y., Zhang, Z., Lin, S., and Guo, B. Swin transformer: Hierarchical vision transformer using shifted windows. In *Proceedings of the IEEE/CVF international conference on computer vision*, pp. 10012–10022, 2021.

Lu, P. D., Nguyen, K., Tran, A., and Nguyen, C. Any3dis: Class-agnostic 3d instance segmentation by 2d mask tracking. In *CVPR*, 2025.

Lu, S., Chang, H., Jing, E. P., Boularias, A., and Bekris, K. Ovir-3d: Open-vocabulary 3d instance retrieval without training on 3d data. In *CoRL*, 2023.

Luo, T., Rockwell, C., Lee, H., and Johnson, J. Scalable 3d captioning with pretrained models. *Advances in Neural Information Processing Systems*, 36:75307–75337, 2023.

Luo, T., Johnson, J., and Lee, H. View selection for 3d captioning via diffusion ranking. In *ECCV*, pp. 180–197. Springer, 2024.

Mei, G., Riz, L., Wang, Y., and Poiesi, F. Vocabulary-free 3d instance segmentation with vision and language assistant. In *International Conference on 3D Vision (3DV)*, 2024.

Ngo, T. D., Hua, B.-S., and Nguyen, K. Isbnet: a 3d point cloud instance segmentation network with instance-aware sampling and box-aware dynamic convolution. In *Proceedings of the IEEE/CVF Conference on Computer Vision and Pattern Recognition*, pp. 13550–13559, 2023.

Nguyen, K., de Silva Edirimuni, D., Hassan, G. M., and Mian, A. Retrieving objects from 3d scenes with box-guided open-vocabulary instance segmentation. *arXiv preprint arXiv:2512.19088*, 2025.

Nguyen, P., Ngo, T. D., Kalogerakis, E., Gan, C., Tran, A., Pham, C., and Nguyen, K. Open3dis: Open-vocabulary 3d instance segmentation with 2d mask guidance. In *Proceedings of the IEEE/CVF Conference on Computer Vision and Pattern Recognition*, pp. 4018–4028, 2024.

Oord, A. v. d., Li, Y., and Vinyals, O. Representation learning with contrastive predictive coding. *arXiv preprint arXiv:1807.03748*, 2018.

Park, C., Jeong, Y., Cho, M., and Park, J. Fast point transformer. In *Proceedings of the IEEE/CVF conference on computer vision and pattern recognition*, pp. 16949–16958, 2022.

Peng, S., Genova, K., Jiang, C., Tagliasacchi, A., Pollefeys, M., Funkhouser, T., et al. Openscene: 3d scene understanding with open vocabularies. In *CVPR*, pp. 815–824, 2023.

Qi, C. R., Su, H., Mo, K., and Guibas, L. J. Pointnet: Deep learning on point sets for 3d classification and segmentation. In *Proceedings of the IEEE conference on computer vision and pattern recognition*, pp. 652–660, 2017.

Qi, L., Kuen, J., Shen, T., Gu, J., Li, W., Guo, W., Jia, J., Lin, Z., and Yang, M.-H. High quality entity segmentation. In *2023 IEEE/CVF International Conference on Computer Vision (ICCV)*, pp. 4024–4033. IEEE, 2023.

Radford, A., Kim, J. W., Hallacy, C., Ramesh, A., Goh, G., Agarwal, S., Sastry, G., Askell, A., Mishkin, P., Clark, J., et al. Learning transferable visual models from natural language supervision. In *International conference on machine learning*, pp. 8748–8763. PmLR, 2021.

Rashid, A., Sharma, S., Kim, C. M., Kerr, J., Chen, L. Y., Kanazawa, A., and Goldberg, K. Language embedded radiance fields for zero-shot task-oriented grasping. In *7th Annual Conference on Robot Learning*, 2023.

Ravi, N., Gabeur, V., Hu, Y.-T., Hu, R., Ryali, C., Ma, T., Khedr, H., Rädle, R., Rolland, C., Gustafson, L., et al. Sam 2: Segment anything in images and videos. In *arXiv preprint arXiv*, 2024.

Ren, T., Liu, S., Zeng, A., Lin, J., Li, K., Cao, H., Chen, J., Huang, X., Chen, Y., Yan, F., et al. Grounded sam: Assembling open-world models for diverse visual tasks. *arXiv preprint arXiv:2401.14159*, 2024.

Rozenberszki, D., Litany, O., and Dai, A. Language-grounded indoor 3d semantic segmentation in the wild. In *European Conference on Computer Vision*, pp. 125–141. Springer, 2022.

Schult, J., Engelmann, F., Hermans, A., Litany, O., Tang, S., and Leibe, B. Mask3d: Mask transformer for 3d semantic instance segmentation. In *2023 IEEE International Conference on Robotics and Automation (ICRA)*, pp. 8216–8223. IEEE, 2023.

Straub, J., Whelan, T., Ma, L., Chen, Y., Wijmans, E., Green, S., Engel, J. J., Mur-Artal, R., Ren, C., Verber, S., Clarkson, J., Yan, Q., Wang, S., Alcantarilla, P., Cabezas, I., Chapin, L., De Nardi, R., Frank, B., Golber, O., Goldman, D., Haenel, P., Kendall, A., Leon, S., Lovegrove, S., Lv, C., Mudrazija, N., Peris, R., Rennie, S., Restrepo, L., Rodriguez, R., Stanton, B., Strauss, A., Sweeney, C., Trope, R., and Zafer, N. The replica dataset: A digital replica of indoor spaces. *arXiv preprint arXiv:1906.05797*, 2019.

Su, J., Ahmed, M., Lu, Y., Pan, S., Bo, W., and Liu, Y. Roformer: Enhanced transformer with rotary position embedding. *Neurocomputing*, 568:127063, 2024.

Takmaz, A., Fedele, E., Sumner, R. W., Pollefeys, M., Tombari, F., and Engelmann, F. Openmask3d: open-vocabulary 3d instance segmentation. In *NIPS*, pp. 68367–68390, 2023.

Tang, Y., Zhang, J., Lan, Y., Guo, Y., Dong, D., Zhu, C., and Xu, K. Onlineanyseg: Online zero-shot 3d segmentation by visual foundation model guided 2d mask merging. In *CVPR*, 2025.

Thomas, H., Qi, C. R., Deschaud, J.-E., Marcotegui, B., Goulette, F., and Guibas, L. J. Kpconv: Flexible and deformable convolution for point clouds. In *Proceedings of the IEEE/CVF international conference on computer vision*, pp. 6411–6420, 2019.

Wang, P.-S. Octformer: Octree-based transformers for 3d point clouds. *ACM Transactions on Graphics (TOG)*, 42(4):1–11, 2023.

Wu, X., Lao, Y., Jiang, L., Liu, X., and Zhao, H. Point transformer v2: Grouped vector attention and partition-based pooling. *Advances in Neural Information Processing Systems*, 35: 33330–33342, 2022.

Wu, X., Jiang, L., Wang, P.-S., Liu, Z., Liu, X., Qiao, Y., Ouyang, W., He, T., and Zhao, H. Point transformer v3: Simpler, faster, stronger. In *CVPR*, 2024.

Xu, X., Huang, H., Li, Y., Liu, N., Lu, Z., et al. Embodiedsam: Online segment any 3d thing in real time. In *ICLR*, 2025.

Yan, M., Zhang, J., Zhu, Y., and Wang, H. Maskclustering: View consensus based mask graph clustering for open-vocabulary 3d instance segmentation. In *Proceedings of the IEEE/CVF Conference on Computer Vision and Pattern Recognition*, pp. 28274–28284, 2024.

Yang, D., Xu, Z., Mo, W., Chen, Q., Huang, S., and Liu, Y. 3d vision and language pretraining with large-scale synthetic data. In *Proceedings of the Thirty-Third International Joint Conference on Artificial Intelligence*, pp. 1552–1560, 2024a.

Yang, J., Ding, R., Deng, W., Wang, Z., and Qi, X. Regionplc: Regional point-language contrastive learning for open-world 3d scene understanding. In *CVPR*, pp. 19823–19832, 2024b.

Yeshwanth, C., Liu, Y.-C., Nießner, M., and Dai, A. Scannet++: A high-fidelity dataset of 3d indoor scenes. In *Proceedings of the IEEE/CVF International Conference on Computer Vision*, pp. 12–22, 2023.

Yin, Y., Liu, Y., Xiao, Y., Cohen-Or, D., Huang, J., and Chen, B. Sai3d: Segment any instance in 3d scenes. In *Proceedings of the IEEE/CVF Conference on Computer Vision and Pattern Recognition*, pp. 3292–3302, 2024.

Zhang, H., Xu, J., Tang, T., Sun, H., Yu, X., Huang, Z., and Yu, K. Opensight: A simple open-vocabulary framework for lidar-based object detection. In *European Conference on Computer Vision*, pp. 1–19. Springer, 2024.

Zhou, X., Girdhar, R., Joulin, A., Krähenbühl, P., and Misra, I. Detecting twenty-thousand classes using image-level supervision. In *ECCV*, 2022.

Zhou, Z., Wei, S., Wang, Z., Wang, C., Yan, X., and Liu, X. Opentrack3d: Towards accurate and generalizable open-vocabulary 3d instance segmentation. *arXiv preprint arXiv:2512.03532*, 2025.

A. Appendix

A.1. 3D Rotary Positional Embeddings (RoPE) - Detailed Mathematics

In this section, we provide a detailed mathematical exposition of the 3D Rotary Positional Embeddings (RoPE) used in our voxel transformer architecture. RoPE directly encodes relative positional information through rotation transformations applied to query and key vectors.

A.1.1. Background: 2D Rotary Embeddings

The original RoPE formulation (Su et al., 2024) was designed for 1D sequences in language models. The key insight is to encode position through rotation of query and key vectors in the complex plane. For a 2D vector $\mathbf{x} = [x_1, x_2]^\top$, a rotation by angle θ can be expressed as:

$$\begin{bmatrix} x_1' \\ x_2' \end{bmatrix} = \begin{bmatrix} \cos\theta & -\sin\theta \\ \sin\theta & \cos\theta \end{bmatrix} \begin{bmatrix} x_1 \\ x_2 \end{bmatrix} \tag{10}$$

Alternatively, treating the vector as a complex number $z = x_1 + ix_2$, rotation becomes multiplication by $e^{i\theta}$:

$$z' = z \cdot e^{i\theta} = (x_1 + ix_2)(\cos\theta + i\sin\theta) \tag{11}$$

A.1.2. Extension to 3D Voxel Space

For 3D voxel data, we extend RoPE to encode positions along three spatial dimensions. The attention score between voxels at positions $\mathbf{p}_i = (x_i, y_i, z_i)$ and $\mathbf{p}_j = (x_j, y_j, z_j)$ is computed as:

$$\langle \mathbf{q}_i, \mathbf{k}_j \rangle = \mathbf{q}_i \mathbf{R}_{\Theta, \mathbf{p}_j - \mathbf{p}_i} \mathbf{k}_j^\top, \tag{12}$$

where $\mathbf{R}_{\Theta,\Delta\mathbf{p}}$ is a block-diagonal rotation matrix parameterized by the relative position $\Delta\mathbf{p} = (x_j - x_i, y_j - y_i, z_j - z_i)$.

Rotation Matrix Structure. The rotation matrix $\mathbf{R}_{\Theta,\Delta\mathbf{p}}$ has a block-diagonal structure:

$$\mathbf{R}_{\Theta,\Delta\mathbf{p}} = \begin{bmatrix} \mathbf{R}_x(\theta_x) & & \\ & \mathbf{R}_y(\theta_y) & \\ & & \mathbf{R}_z(\theta_z) \end{bmatrix}, \tag{13}$$

where each $\mathbf{R}_d(\theta_d)$ for $d \in \{x, y, z\}$ consists of multiple 2D rotation blocks applied to pairs of feature dimensions.

Frequency Computation. For feature dimension d_h (head dimension), we allocate dimensions equally among the three spatial axes. Each spatial dimension uses $d_{\text{rope}}/3$ dimensions where:

$$d_{\text{rope}} = \left\lfloor \frac{d_h}{6} \right\rfloor \times 6 \tag{14}$$

The rotation angles are computed using position-dependent frequencies:

$$\theta_d^{(m)} = \frac{\Delta p_d}{\text{base}^{2m/(d_{\text{rope}}/3)}}, \quad m \in \{0, 1, \ldots, d_{\text{rope}}/6 - 1\} \tag{15}$$

where base (typically 10^4) controls the wavelength of the sinusoidal embeddings, and Δp_d is the relative position difference along dimension d.

A.1.3. Application to Query and Key Vectors

Given query and key vectors $\mathbf{q}, \mathbf{k} \in \mathbb{R}^{d_h}$, the rotation matrix $\mathbf{R}_{\Theta,\Delta\mathbf{p}}$ operates on pairs of dimensions. Specifically, each $\mathbf{R}_d(\theta_d)$ for $d \in \{x, y, z\}$ is composed of $d_{\text{rope}}/6$ independent 2D rotation matrices:

$$\mathbf{R}_d(\theta_d) = \text{diag}\left(\mathbf{R}_d^{(0)}, \mathbf{R}_d^{(1)}, \ldots, \mathbf{R}_d^{(d_{\text{rope}}/6-1)}\right), \tag{16}$$

where each 2D rotation block is:

$$\mathbf{R}_d^{(m)} = \begin{bmatrix} \cos\theta_d^{(m)} & -\sin\theta_d^{(m)} \\ \sin\theta_d^{(m)} & \cos\theta_d^{(m)} \end{bmatrix} \tag{17}$$

The complete transformation can be written as:

$$\mathbf{q}' = \mathbf{R}_{\Theta,\Delta\mathbf{p}}\mathbf{q} = \begin{bmatrix} \mathbf{R}_x(\theta_x) & & & \\ & \mathbf{R}_y(\theta_y) & & \\ & & \mathbf{R}_z(\theta_z) & \\ & & & \mathbf{I}_{d_h - d_{\text{rope}}} \end{bmatrix} \mathbf{q} \tag{18}$$

where $\mathbf{I}_{d_h - d_{\text{rope}}}$ is an identity matrix for dimensions not affected by RoPE.

A.1.4. Properties of 3D RoPE

Relative Position Encoding. The key property of RoPE is that the attention score between two voxels depends only on their relative position:

$$\langle \mathbf{q}_i, \mathbf{k}_j \rangle = \mathbf{q}_i \mathbf{R}_{\Theta,\mathbf{p}_j - \mathbf{p}_i} \mathbf{k}_j^\top = f(\mathbf{q}_i, \mathbf{k}_j, \Delta\mathbf{p}_{ij}) \tag{19}$$

where $\Delta\mathbf{p}_{ij} = \mathbf{p}_j - \mathbf{p}_i = (x_j - x_i, y_j - y_i, z_j - z_i)$ is the relative position vector.

Translation Invariance. The attention scores are invariant to global translations. If all voxel positions are shifted by $\mathbf{t} = (t_x, t_y, t_z)$:

$$\langle \mathbf{q}_i, \mathbf{k}_j \rangle_{\mathbf{p}+\mathbf{t}} = \langle \mathbf{q}_i, \mathbf{k}_j \rangle_{\mathbf{p}} \tag{20}$$

This property ensures that the model learns spatial patterns independent of absolute position in the scene.

Long-Range Decay. The positional encoding naturally decays for distant voxels due to the periodic nature of the sinusoidal functions, helping the model focus on local spatial relationships while maintaining awareness of global structure.

A.1.5. Implementation Details

In practice, our implementation includes several optimizations:

1. **On-the-fly computation**: Unlike language models that can cache positional embeddings for fixed sequence positions, we compute RoPE dynamically for each voxel's coordinates, as sparse voxel data can have arbitrary coordinate values.

2. **Coordinate normalization**: To handle large coordinate values, we normalize by subtracting the minimum coordinate in each batch:

$$\tilde{x}_i = x_i - \min_j(x_j) + 1 \tag{21}$$

3. **Learnable frequencies**: Optionally, the frequency parameters θ_j can be made learnable:

$$\theta_j = \text{softplus}(\mathbf{w}_j)/\text{base}^{2j/(d_{\text{rope}}/3)} \tag{22}$$

where $\mathbf{w}_j$ are learnable parameters.

A.1.6. Comparison with Alternative Position Encodings

Table 10 compares 3D RoPE with alternative positional encoding methods for voxel data:

The key advantages of 3D RoPE are:

- **No additional parameters**: Position information is encoded through rotation, not learned embeddings
- **Better extrapolation**: Can handle coordinate ranges not seen during training
- **Computational efficiency**: No need to store large positional embedding tables
- **Natural 3D structure**: Separately encodes x, y, z dimensions while maintaining their relationships

Table 10. Comparison of positional encoding methods for 3D voxel transformers

Method	Translation Invariant	Memory Efficient	Extrapolation
Additive sinusoidal PE	✗	✓	✗
Learnable PE	✗	✗	✗
Relative PE	✓	✗	✓
3D RoPE (ours)	✓	✓	✓

A.2. Window Attention with RoPE

When applying RoPE within windowed attention, special care must be taken to preserve relative position information. For each window $\mathcal{W}_i$ containing voxels with positions $\{\mathbf{p}_1, \mathbf{p}_2, \ldots, \mathbf{p}_{|\mathcal{W}_i|}\}$:

1. **Global coordinate preservation**: We use the original voxel positions, not window-local indices. The attention computation within window $\mathcal{W}_i$ is:

$$\langle \mathbf{q}_m, \mathbf{k}_n \rangle = \mathbf{q}_m \mathbf{R}_{\Theta, \mathbf{p}_n - \mathbf{p}_m} \mathbf{k}_n^\top \quad \forall v_m, v_n \in \mathcal{W}_i \tag{23}$$

2. **Cross-window consistency**: The rotation matrix $\mathbf{R}_{\Theta,\Delta\mathbf{p}}$ depends only on the relative position $\Delta\mathbf{p}$, ensuring consistent encoding regardless of window assignment.

3. **Window-aware normalization**: When normalizing coordinates to handle large values, we use global statistics:

$$\tilde{\mathbf{p}}_j = \mathbf{p}_j - \min_{k \in \text{batch}} (\mathbf{p}_k) + \mathbf{1} \tag{24}$$

where $\mathbf{1} = (1, 1, 1)$ ensures non-zero positions.

This design ensures that relative positions between voxels are preserved even when they are assigned to different windows, maintaining the translation invariance property of RoPE.

A.3. RoPE in Instance Segmentation Decoder: Complete Formulation

This section provides the complete mathematical formulation of RoPE in the instance segmentation decoder (Sec. 4.4), including detailed cross-attention equations, self-attention formulations, and analysis of the benefits.

A.3.1. Detailed Cross-Attention Formulation

At iteration t, we randomly sample S points from the scene to form keys and values. Let $\mathcal{S}_t \subseteq \{1, \ldots, N\}$ denote the sampled indices with corresponding CLIP features $\mathbf{F}_{\text{CLIP},s} = \{\mathbf{f}_{s_j}^{\text{clip}}\}_{j=1}^S$ and coordinates $\mathbf{P}_s = \{\mathbf{p}_{s_j}\}_{j=1}^S$. For cross-attention, we apply RoPE rotations $\mathcal{R}(\mathbf{x}, \mathbf{p})$ to both queries and keys based on their 3D coordinates:

$$\widetilde{\mathbf{Q}}^{(t)} = \{\mathcal{R}(\mathbf{W}_Q \mathbf{q}_i^{(t)}, \mathbf{p}_{q,i})\}_{i=1}^Q, \tag{25}$$

$$\widetilde{\mathbf{K}}_s = \{\mathcal{R}(\mathbf{W}_K \mathbf{f}_{s_j}^{\text{clip}}, \mathbf{p}_{s_j})\}_{j=1}^S, \tag{26}$$

$$\mathbf{V}_s = \mathbf{W}_V \mathbf{F}_{\text{CLIP},s}, \tag{27}$$

$$\mathbf{A}^{(t)} = \text{Softmax}\left(\frac{\widetilde{\mathbf{Q}}^{(t)} \widetilde{\mathbf{K}}_s^\top}{\sqrt{d_h}} + \mathbf{M}^{(t)}\right), \tag{28}$$

$$\mathbf{Q}^{(t+0.5)} = \mathbf{A}^{(t)} \mathbf{V}_s, \tag{29}$$

where $\mathbf{W}_Q, \mathbf{W}_K, \mathbf{W}_V$ are learned projection matrices, d_h is the head dimension, and $\mathbf{M}^{(t)} \in \{0, -\infty\}^{Q \times S}$ is an attention mask computed from predicted instance masks to focus queries on relevant regions.

Key Difference from Backbone RoPE. In the backbone (Sec. 4.3), RoPE encodes the relative displacement $\mathbf{p}_j - \mathbf{p}_i$ between voxels within a local window. However, in the decoder, queries represent *instance proposals* at specific spatial locations, and we need to preserve their absolute positions to distinguish between instances at different locations. Therefore,

we apply RoPE using absolute coordinates—rotating queries and keys independently by $\mathcal{R}(\cdot, \mathbf{p}_i)$ and $\mathcal{R}(\cdot, \mathbf{p}_j)$ respectively. Due to rotation matrix properties, this still captures relative positions while preserving absolute spatial information in the feature representations.

A.3.2. Self-Attention with RoPE

After cross-attention, queries interact through self-attention to model relationships between instance proposals. We apply RoPE to the self-attention queries and keys using the fixed query coordinates $\mathbf{P}_q$:

$$\widetilde{\mathbf{Q}}_{\text{self}}^{(t)} = \{\mathcal{R}(\mathbf{W}_Q^s \mathbf{q}_i^{(t+0.5)}, \mathbf{p}_{q,i})\}_{i=1}^{Q}, \tag{30}$$

$$\widetilde{\mathbf{K}}_{\text{self}}^{(t)} = \{\mathcal{R}(\mathbf{W}_K^s \mathbf{q}_i^{(t+0.5)}, \mathbf{p}_{q,i})\}_{i=1}^{Q}, \tag{31}$$

$$\mathbf{Q}^{(t+0.75)} = \text{SelfAttn}(\widetilde{\mathbf{Q}}_{\text{self}}^{(t)}, \widetilde{\mathbf{K}}_{\text{self}}^{(t)}), \tag{32}$$

where $\mathbf{W}_Q^s, \mathbf{W}_K^s$ are self-attention projection matrices. This allows queries to be spatially aware of their locations when interacting, enabling the model to learn that nearby queries should cooperate (e.g., for parts of the same object) while distant queries can specialize independently.

A.3.3. Complete Iterative Refinement

After self-attention, a feed-forward network further processes the queries:

$$\mathbf{Q}^{(t+1)} = \text{FFN}(\mathbf{Q}^{(t+0.75)}) + \mathbf{Q}^{(t+0.75)}. \tag{33}$$

This process repeats for T iterations (typically $T = 3$ in our experiments) with shared weights across iterations, allowing progressive refinement of instance proposals.

A.3.4. Benefits of RoPE in Instance Segmentation

Integrating RoPE into the instance segmentation decoder provides several advantages:

(1) Spatial Awareness: RoPE enables queries to be spatially aware during both cross-attention (when attending to scene features) and self-attention (when interacting with other queries). This is crucial for instance segmentation, where the spatial location of a proposal determines which scene regions it should attend to.

(2) Absolute Position Encoding: Unlike relative position encoding in the backbone, absolute position encoding in the decoder allows the model to distinguish between instances at different spatial locations, preventing ambiguity when multiple instances of the same category exist.

(3) Geometry-Aware Reasoning: By encoding 3D coordinates directly into the attention mechanism, RoPE helps the model reason about geometric relationships—for example, queries at similar heights are more likely to belong to similar object categories (tables, chairs) than queries at very different heights (floor, ceiling).

(4) Extrapolation: RoPE's continuous nature allows the model to generalize to scenes larger than those seen during training, as the rotation angles smoothly vary with coordinate values.

A.4. Attention Normalization

The placement of layer normalization (LN) within attention blocks is a critical design choice that affects training stability and performance. We consider three variants: Default, PreNorm, and PostNorm architectures, which differ in both the placement of normalization and the source of residual connections.

Default architecture. In the default variant, layer normalization is applied to the input before it branches into attention or MLP operations, and the residual connections use the normalized values:

$$\widetilde{\mathbf{C}}^l = \text{LN}(\mathbf{C}^l), \tag{34}$$

$$\mathbf{A}^l = \text{MHSA}(\widetilde{\mathbf{C}}^l) + \widetilde{\mathbf{C}}^l, \tag{35}$$

$$\widetilde{\mathbf{A}}^l = \text{LN}(\mathbf{A}^l), \tag{36}$$

$$\mathbf{H}^l = \text{FFN}(\widetilde{\mathbf{A}}^l) + \widetilde{\mathbf{A}}^l, \tag{37}$$

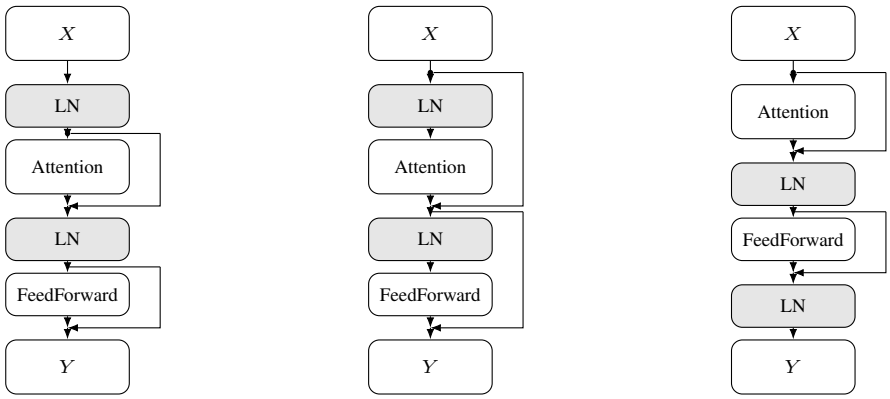

(a) Default *(b)* PreNorm *(c)* PostNorm

Figure 11. **Attention normalization variants.** (Left to right) Default, PreNorm, and PostNorm attention block architectures. Default applies LayerNorm (LN) before branching into attention/MLP, with residuals from normalized values. PreNorm applies LN inline before operations, with residuals from original values. PostNorm applies LN after operations and residual additions. Residual connections are shown with skip paths.

where $\mathbf{C}^l$ is the convolved feature from the previous layer, MHSA is multi-head self-attention, FFN is the feed-forward network, and LN denotes layer normalization. This variant applies normalization before branching, ensuring both the operation and residual use normalized inputs.

PreNorm architecture. In the PreNorm variant, layer normalization is applied inline before the operations, but the residual connections use the original (unnormalized) values:

$$\mathbf{A}^l = \text{MHSA}(\text{LN}(\mathbf{C}^l)) + \mathbf{C}^l, \tag{38}$$

$$\mathbf{H}^l = \text{FFN}(\text{LN}(\mathbf{A}^l)) + \mathbf{A}^l. \tag{39}$$

This is the standard PreNorm architecture used in modern transformers such as Vision Transformer (ViT) and is known for its training stability, especially in deep networks. The key difference from the default variant is that residuals come from the original values before normalization.

PostNorm architecture. In the PostNorm variant, layer normalization is applied after the attention and feed-forward operations and their residual additions:

$$\mathbf{A}^l = \text{LN}(\text{MHSA}(\mathbf{C}^l) + \mathbf{C}^l), \tag{40}$$

$$\mathbf{H}^l = \text{LN}(\text{FFN}(\mathbf{A}^l) + \mathbf{A}^l). \tag{41}$$

The PostNorm architecture was used in the original Transformer paper and can provide different gradient flow characteristics, though it may require more careful initialization and learning rate scheduling for deep networks.

Implementation. Our framework supports all three variants through the `AttentionBlock`, `AttentionBlockPreNorm`, and `AttentionBlockPostNorm` classes, allowing for empirical comparison of normalization strategies in 3D vision transformers. We apply these designs consistently in both backbone and decoder blocks. The PreNorm variant is used as the default in our experiments due to its superior training stability, which we found particularly important for end-to-end training of our *proposal-free* instance segmentation model.

A.5. Additional Method Details

A.5.1. Spatial Coherence Metric

To quantify the spatial coherence improvement, we measure the average pairwise distance between voxels within the same attention window. For a window $\mathcal{W}$ containing n voxels, the spatial coherence is defined as:

$$C(\mathcal{W}) = \frac{1}{\binom{n}{2}} \sum_{i=1}^{n} \sum_{j=i+1}^{n} \|\mathbf{p}_i - \mathbf{p}_j\|_2, \tag{42}$$

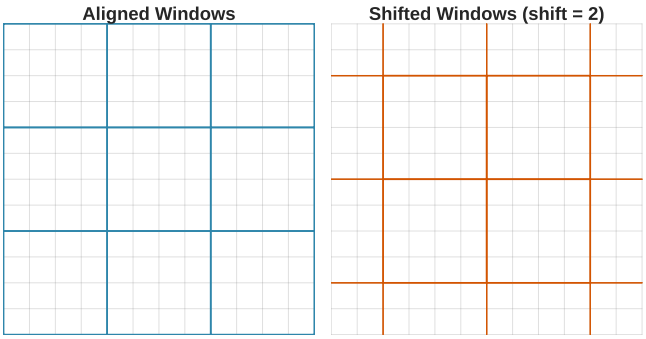

Figure 12. **SWIN Windowing on a 2D Grid.** (Left) Non-overlapping windows aligned to the grid. (Right) Non-overlapping windows shifted by half the window size, illustrating SWIN's shifted windowing.

where $\mathbf{p}_i = (x_i, y_i, z_i)$ and $\mathbf{p}_j = (x_j, y_j, z_j)$ are the 3D coordinates of voxels v_i and v_j in window $\mathcal{W}$. Lower values indicate better spatial coherence.

A.5.2. Window Attention Implementation

We operate spatial window attention in 3D cubic windows of shape $H \times W \times D$ voxels. For each window, we compute per-head queries, keys, and values only on the active voxels inside the cube. A window mask $\mathbf{M}$ restricts interactions to within the cube, ignoring padded or empty positions. Morton code attention uses fixed-length segments as described in (Wu et al., 2024). Both mechanisms scan the entire space while maintaining local interactions.

A.5.3. Shifted Window Attention

To enable cross-window connections and prevent overfitting to a fixed grid, we adopt a randomized shifted windowing scheme. Unlike the deterministic alternating shifts in Swin Transformer (Liu et al., 2021), we randomly sample a shift configuration for each layer. The window partition can be shifted by half the window size ($W/2$) along any combination of axes: x, y, z, xy, xz, yz, or xyz. Formally, for each axis $d \in \{x, y, z\}$, the shift is independently chosen as either 0 or $W_d/2$.

Formally, for sliding windows with stride s and window dimensions (W_x, W_y, W_z), we define:

$$\begin{aligned} \mathcal{W}^{\text{sliding}}_{(a,b,c)} = \{v_i : & as \leqslant x_i < as + W_x, \\ & bs \leqslant y_i < bs + W_y, \\ & cs \leqslant z_i < cs + W_z\}, \end{aligned} \tag{43}$$

where (a, b, c) are indices along each axis. This ensures voxels in the same spatial neighborhood are processed together.

A.5.4. Space-Curve Attention Pseudocode

Algorithm 1 summarizes our space-curve attention strategy, which combines spatial window attention and Morton curve attention at each encoder/decoder level.

A.6. Dataset Generation Details

Data Processing Details. We implement standardized preprocessing modules for the major indoor scene datasets.

- **ScanNet**: We parse the proprietary `.sens` format using a custom SensorData reader, extracting JPEG-compressed color frames and zlib-compressed depth maps at two-frame intervals. Camera poses are derived from the sensor's camera-to-world matrices, and intrinsics are scaled according to the target resolution (default: 640px maximum dimension).
- **ARKitScenes**: We process trajectory files containing angle-axis pose representations, converting them to 4×4 transformation matrices. Device orientation changes are handled by detecting rotations and applying appropriate image rotations (0°, 90°, 180°, 270°) using OpenCV transforms.

Algorithm 1 Space-Curve Attention

Require: Voxel features $\mathbf{H} \in \mathbb{R}^{N \times d}$, coords $\mathbf{P} \in \mathbb{R}^{N \times 3}$, level ℓ
if level ℓ uses spatial windows **then**
  Sample random shift $\delta \in \{0, W_\ell/2\}^3$
  $\{\mathcal{W}_k\} \leftarrow \textsc{SpatialPartition}(\mathbf{P} + \delta, W_\ell)$
  for each window $\mathcal{W}_k$ **do**
    $\mathbf{Q}, \mathbf{K}, \mathbf{V} \leftarrow$ project($\mathbf{H}[\mathcal{W}_k]$)
    Apply 3D RoPE to $\mathbf{Q}, \mathbf{K}$ with relative positions
    $\mathbf{H}[\mathcal{W}_k] \leftarrow \text{MHSA}(\mathbf{Q}, \mathbf{K}, \mathbf{V})$
  end for
else
  $\pi \leftarrow \textsc{MortonSerialize}(\mathbf{P})$
  Partition π into fixed-length segments of size L
  for each segment $\mathcal{S}_k$ **do**
    $\mathbf{Q}, \mathbf{K}, \mathbf{V} \leftarrow$ project($\mathbf{H}[\mathcal{S}_k]$)
    Apply 3D RoPE to $\mathbf{Q}, \mathbf{K}$ with relative positions
    $\mathbf{H}[\mathcal{S}_k] \leftarrow \text{MHSA}(\mathbf{Q}, \mathbf{K}, \mathbf{V})$
  end for
end if
return $\mathbf{H}$

- **ScanNet++**: We utilize COLMAP reconstructions, parsing `images.txt` to extract quaternion-based poses and converting them to world-to-camera matrices. We integrate with NeRFStudio-format transforms to extract intrinsics from `transforms_undistorted.json`.

- **Matterport3D**: We apply spatial filtering based on point cloud bounding boxes to select relevant viewpoints. Separate pose and intrinsic files are converted from Matterport's coordinates to our standardized format while maintaining a depth scale factor of 4000.0.

Overlap-based View Sampling. We compute overlap between consecutive frames via backproject depth to obtain per-frame point clouds.

$$\bigcap(\mathcal{P}_{t_i}, \mathcal{P}_{t_j}) = \frac{1}{|\mathcal{P}_{t_i}|} \sum_{p \in \mathcal{P}_{t_i}} \mathbb{1}\left[\min_{q \in \mathcal{P}_{t_j}} \|p - q\|_2 < \varepsilon\right], \tag{44}$$

where $\mathcal{P}_{t_i} \in \mathbb{R}^{HW \times 3}$ is the backprojected per-frame point cloud at timestep t_i, $\mathbb{1}[\cdot]$ is the indicator function, and ε is a 3D proximity threshold.

View Selection for Captioning. We select up to K representative views using weighted k-medoids clustering over the temporal dimension. The distance matrix is $D_{jk} = |t_j - t_k|$ for frame timestamps, with weights $w_j = \sum_{p \in M_i^j} \mathbb{1}[p \in M_i^j]$ corresponding to mask pixel count in each view. This weighting scheme prioritizes frames with high instance visibility while maintaining temporal spread, ensuring informative viewpoints for caption generation.

Quality Control. The slight missing caption files (13 out of 15,880 total) in ScanNet++ and Matterport3D represent scenes that failed post-processing quality checks due to insufficient multi-view support or depth quality issues. These exclusions constitute less than 0.1% of the total data and do not affect overall dataset integrity. All remaining mask-caption pairs pass our geometric consistency and multi-view agreement thresholds established in the aggregation pipeline.

A.7. Multi-view Captioning Details

In this section, we provide the full system prompt, user prompt, and additional examples of the multi-view captioning process described in Sec. 3.

A.7.1. System Prompt

The following system prompt is used to instruct the VLM (Gemma 3) to generate intrinsic and spatially consistent captions:

Full System Prompt

You are an expert image-captioning assistant. You will be given multiple "views" of the same subject. Your job is to synthesize these views into one cohesive description that focuses on the subject's intrinsic properties. Note that this "object" might actually be a wall, floor, or part of a larger structure—so it may not always be a standalone, traditional object. In such cases, describe the subject as best you can (color, texture, material, shape, typical size, etc.):
Object Properties

- Emphasize color, shape, material, texture, and typical size (e.g., small, medium, large).
- If uncertain about the object type, use best judgment (e.g., "a piece of fabric" could be "a pillow" if it looks stuffed).

Relationships to Other Objects

- Only mention other objects if they appear consistently across all views.
- At the end of your description, state how the foreground object is related spatially to these other objects (e.g., "It is on a table with a blue vase and a green plant").
- Do not mention the camera's or viewer's position (e.g., "top-left corner," "on the right side").

What Not to Mention

- Do not mention bounding boxes, outlines, image padding, or differences between views (e.g., "In the first image...").
- Do not describe masked cutouts or the act of masking—they are merely visualization aids.

Output Format

- Provide a single concise paragraph that directly describes the object.
- Avoid filler phrases such as "The object is..." or "In the image...".
- End with a short sentence describing its spatial relationship to other objects (if any).

Example: "A medium-sized red ceramic vase with a smooth, glossy finish. It has a narrow neck and a rounded body. It is on a table with a blue vase and a green plant."
Note: Each image is labeled "View N: ...". Any images sharing the same N come from the same original viewpoint (e.g., different mask types or outlines for the same photo).

A.7.2. User Prompt and Example

We allow the user prompt to handle the multi-view logic. Below is the user prompt template and a sample assistant response.

User Prompt

Describe the object shown across all views and its relationship to other objects in the scene. Do not describe location relative to the viewpoint or image as the captions will be used for 3D datasets which will combine all camera views. Some object may be located within another object, such as a bag in a cabinet. Disregard the background and focus on the foreground object. View 1: A cropped view of the object with a red outline drawn around it: `<IMAGE_1>`. View 1: A cutout/mask that isolates the foreground object and hides the background: `<IMAGE_2>`. View 2: A cropped view of the object with a red outline drawn around it: `<IMAGE_3>`. View 2: A cutout/mask that isolates the foreground object and hides the background: `<IMAGE_4>`.

Assistant Caption

A tall, slender musical instrument with a light brown, wooden body and neck. It features a rectangular sound box with decorative carvings and a long, curved neck extending upwards. It is situated on a wooden surface near a fan and a cabinet.

A.7.3. Additional Examples

Figure 3 in the main text illustrates the pipeline for a musical instrument.

A.8. Additional Dataset Examples

In this section, we provide additional examples of 3D instance masks and their corresponding captions from our SpaCeFormer-3M dataset. These examples demonstrate the diversity of scenes, objects, and caption quality across different environments

including office/lounge areas, communal waiting rooms, bedrooms, and retail spaces.

(1) "A small, dark wood nightstand provides storage near the bed, featuring brass-toned hardware and a traditional design."
(2) "The reddish-brown bedside table sits adjacent to the bed, its rectangular shape complementing the room's layout."
(3) "This medium-sized wooden cabinet offers a surface for lamps and books, easily accessible from the bed."
(4) "Crafted from wood with a visible grain, the nightstand's design blends classic style with functional storage."
(5) "The dark brown nightstand, positioned next to the bed, provides a convenient spot for personal items and a lamp."

(1) "The pillow's woven fabric offers a soft, comfortable surface for resting."
(2) "A rectangular pillow with a muted brown and black checkered pattern rests against the bed."
(3) "Medium-sized pillow, suitable for supporting the head during sleep or relaxation."
(4) "The pillow's design complements the bedroom's decor, providing a cozy accent."
(5) "Positioned against the headboard, the pillow offers support and adds visual texture to the bed."

(1) "Dark brown wooden table with ornate carved details, providing a surface for small items."
(2) "Rectangular table with a glossy finish, positioned near a curtain and a chair."
(3) "Medium-sized table offering a flat surface for holding stationery and decorative objects."
(4) "The table's design features cabriole legs and a drawer, blending into the room's decor."
(5) "A dark wood table sits adjacent to a chair, providing a functional space for writing or display."

(1) "The chair's dark fabric upholstery provides a comfortable seating surface, designed for supporting a person."
(2) "A medium-sized chair with a curved backrest sits adjacent to a dark wooden desk, displaying a classic design."
(3) "This chair offers a place to sit; its slender frame allows for easy movement around the room, suitable for quick tasks."
(4) "The chair's metal legs and dark fabric seat create a simple, functional design, blending into the room's decor."
(5) "Positioned near a desk, the chair's dark color contrasts with the lighter carpet, offering a spot for focused work."

Figure 13. **Bedroom Scene Examples.** Traditional bedroom furniture including a nightstand, pillow, ornate table, and desk chair. Captions highlight fine-grained details such as material texture (woven fabric, wood grain), decorative elements (brass hardware, carved details, checkered pattern), and spatial arrangements (near bed, adjacent to desk).

A.9. Detailed Training Objectives

In this section, we provide the detailed mathematical formulations for the training objectives summarized in Sec. 4.4.

A.9.1. Hungarian Matching Cost

Let $\{\mathbf{m}_q\}_{q=1}^{Q}$ be the predicted instance masks (columns of $\mathbf{M} \in \mathbb{R}^{N\times Q}$) and $\{\hat{\mathbf{m}}_k\}_{k=1}^{K}$ the ground-truth instance masks. We assign ground-truth instances to queries via bipartite matching using the Hungarian algorithm. The matching cost $\mathcal{C}(q,k)$ between query q and ground truth k is a weighted sum of classification, mask, and Dice costs (Cheng et al., 2022):

$$\mathcal{C}(q,k) \;=\; \lambda_{\text{class}}\,\mathcal{C}_{\text{class}}(q,k) \;+\; \lambda_{\text{mask}}\,\mathcal{L}_{\text{bce}}(\mathbf{m}_q,\hat{\mathbf{m}}_k) \;+\; \lambda_{\text{dice}}\,(1-\text{Dice}(\mathbf{m}_q,\hat{\mathbf{m}}_k)).$$

Here $\mathcal{C}_{\text{class}}$ uses the query foreground/background probabilities, and $\mathcal{L}_{\text{bce}}$ denotes the sigmoid binary cross-entropy loss.

A.9.2. Loss Components

Mask Loss. For matched pairs $(q,k) \in \mathcal{M}$, we optimize a combination of sigmoid BCE and Dice loss on the per-point mask probabilities:

$$\mathcal{L}_{\text{mask}} \;=\; \sum_{(q,k)\in\mathcal{M}} \left[\lambda_{\text{bce}}\,\mathcal{L}_{\text{bce}}(\mathbf{m}_q,\hat{\mathbf{m}}_k) + \lambda_{\text{dice}}\,\mathcal{L}_{\text{dice}}(\mathbf{m}_q,\hat{\mathbf{m}}_k)\right].$$

where $\mathcal{L}_{\text{dice}}(\mathbf{m},\hat{\mathbf{m}}) = 1 - \frac{2\sum_i m_i\hat{m}_i}{\sum_i m_i + \sum_i \hat{m}_i}$ is the Dice loss.

CLIP Alignment (Contrastive). We align the predicted CLIP features $\mathbf{Z}_q$ (obtained via a linear projection $\mathbf{Z}_q = \mathbf{W}_{\text{CLIP}}\mathbf{Q}^{(T)}$) to target CLIP embeddings $\{\mathbf{t}_k\}$ via an InfoNCE objective (Oord et al., 2018). We compute the alignment probability $p(k|q)$ using a softmax over cosine similarities:

$$p(k|q) = \frac{\exp(\cos(\mathbf{Z}_q,\mathbf{t}_k)/\tau)}{\sum_{k'}\exp(\cos(\mathbf{Z}_q,\mathbf{t}_{k'})/\tau)}.$$

(1) "Woven basket with a rustic texture, ideal for storing small items or displaying decorative objects."
(2) "Brown rectangular box with a dark strap, situated near a wooden crate and potted plant."
(3) "Medium-sized storage box, offering a place to keep belongings organized and easily accessible."
(4) "Handwoven wicker construction, blending seamlessly with the room's natural aesthetic and wooden flooring."
(5) "Dark brown basket, positioned beside a wooden crate, providing a functional and decorative element."

(1) "Dark, rectangular shelf made of composite material, providing storage space above a bench."
(2) "Black shelf with a flat surface, positioned on a wall near clothing racks and a plant."
(3) "Small, wall-mounted shelf offering a place to display decorative items or small objects."
(4) "The shelf's simple, angular design complements the minimalist interior decor, offering a clean aesthetic."
(5) "A dark shelf, slightly angled, sits above a bench, creating a layered display area within the retail space."

(1) "Cream-colored curtains with a soft, flowing texture, likely made of linen or a similar fabric, hang near a window."
(2) "The light beige curtains form a vertical drape, positioned beside a wicker chair and a potted plant."
(3) "These medium-length curtains offer privacy and diffuse light, suitable for a bedroom or living space."
(4) "The curtains' simple design complements the room's decor, creating a calming and inviting atmosphere."
(5) "The fabric drapes gracefully, partially obscuring a window and providing a soft backdrop to the room's furnishings."

(1) "The shelf is constructed from dark brown wood, providing a surface for displaying items."
(2) "A medium-sized, rectangular shelf sits beneath a hanging rack, its gray finish blending with the room's decor."
(3) "This shelf offers a small space for storage or display, easily accessible near the clothing rack."
(4) "The shelf's simple, linear design complements the minimalist aesthetic of the bedroom setting, offering a practical surface."
(5) "Positioned next to a woven basket, the dark gray shelf provides a stable platform for decorative objects and small items."

Figure 14. **Retail/Bedroom Scene Examples.** Mixed-use space with storage and display elements including a woven basket, wall-mounted shelf, curtains, and storage shelf. Captions capture material composition (wicker, composite, linen, wood), functional purposes (storage, display, privacy), and aesthetic qualities (rustic, minimalist, calming atmosphere).

We then maximize the similarity of matched pairs by minimizing the negative log-likelihood:

$$\mathcal{L}_{\text{CLIP}} \;=\; -\sum_{(q,k)\in\mathcal{M}} \log p(k|q).$$

Note that this differs from masked pooling approaches; we directly learn to predict CLIP features from the query embeddings.

Query Foregroundness. We supervise the query objectness scores $\mathbf{C} \in \mathbb{R}^{Q\times 2}$ with a binary label indicating whether a query is matched to any ground truth, using a 2-way cross-entropy loss:

$$\mathcal{L}_{\text{fg}} \;=\; \text{CE}(\mathbf{C}, \mathbf{y}_{\text{fg}}).$$

Optional Closed-Set Semantic Head. When enabled, we apply cross-entropy over the backbone per-voxel logits $\mathbf{Y}$ with ground-truth semantic labels $\hat{\mathbf{y}}$:

$$\mathcal{L}_{\text{sem}} \;=\; \text{CE}(\mathbf{Y}, \hat{\mathbf{y}}).$$

A.10. Muon Optimization Details

Muon performs standard SGD with momentum to obtain an update matrix G, and then post-processes G with a Newton–Schulz iteration that approximately orthogonalizes the update (i.e., replaces G by the nearest semi-orthogonal matrix) before applying it to the parameters. This orthogonalization is implemented efficiently with a quintic Newton–Schulz map and runs stably in bfloat16 on modern GPUs.

Let g_t be the gradient of a 2D parameter (or a batch of 2D parameters) at step t. Muon maintains a momentum buffer m_t and forms an SGD–Nesterov update

$$m_t = \beta\, m_{t-1} + (1-\beta)\, g_t, \qquad G_t = (1-\beta)\, g_t + \beta\, m_t, \tag{45}$$

where G_t has shape $n \times m$ along its last two dimensions. Muon then approximately orthogonalizes G_t via a Newton–Schulz (NS) iteration. Define the initialization

$$X_0 = \frac{G_t}{\|G_t\|_F + \varepsilon}, \tag{46}$$

Algorithm 2 ZeroPower via Newton–Schulz

Require: $G \in \mathbb{R}^{\cdots \times n \times m}$, steps N, (a, b, c), $\varepsilon{>}0$
$X \leftarrow G$; if $n{>}m$ then $X \leftarrow X^\top$
$X \leftarrow X/(\|X\|_F + \varepsilon)$
for $k{=}1..N$ **do**
  $A \leftarrow XX^\top; \quad X \leftarrow aX + (bA + cA^2)X$
end for

return X if $n{\le}m$ else $X^\top$

Algorithm 3 Muon step for one parameter

Require: W, gradient g, momentum m, lr η, decay λ, β, steps N
$m \leftarrow \beta m + (1{-}\beta)g$
$G \leftarrow (1{-}\beta)g + \beta m$
View last two dims as matrix: conv $\rightarrow K{\times}C_{in}{\times}C_{out}$; MoE $\rightarrow E{\times}C_1{\times}C_2$
$\tilde{G} \leftarrow \text{ZeroPower-NS}(G, N)$
$\tilde{G} \leftarrow \tilde{G} \cdot \sqrt{\max(1, n/m)}$
$W \leftarrow (1{-}\eta\lambda)W$
$W \leftarrow W{-}\eta\,\tilde{G}$

and iterate for $k = 0, \ldots, N-1$ (with $N = 5$ in our experiments):

$$A_k = X_k X_k^\top, \tag{47}$$

$$X_{k+1} = aX_k + (\, bA_k + cA_k^2 \,)X_k. \tag{48}$$

With coefficients $(a, b, c) = (3.4445, -4.7750, 2.0315)$, this quintic NS map drives the singular values toward ≈ 1 and yields an update close to the nearest semi-orthogonal matrix to G_t (Jordan et al., 2024). Denoting the SVD $G_t = USV^\top$ and the elementwise polynomial $\varphi(x) = ax + bx^3 + cx^5$, one step produces $U\varphi(S)V^\top$; repeated composition φ^N sharpens singular values toward unity. The implementation uses bfloat16 arithmetic and batched matrix operations.

Finally, we apply a shape correction factor to balance tall versus wide matrices and weight decay/learning-rate scaling when updating the parameter. Our implementation function is `zeropower_via_newtonschulz`, which applies the above NS iteration to the last two dimensions (supporting batched inputs) before the parameter update. Algorithm 2 summarizes the orthogonalization routine and Algorithm 3 shows a per-parameter Muon update.

Batched parameterization for Muon. Muon operates on 2D matrices along their last two dimensions and naturally supports batched matrices via leading dimensions. To make convolutional kernels weights compatible while leveraging this batching, we re-parameterize them as follows:

- **Convolutions**: we arrange each 3D kernel into a tensor of shape $K \times C_{\text{in}} \times C_{\text{out}}$, where K is the product of spatial kernel sizes (e.g., $k_x k_y k_z$). This yields a batch of K matrices of size $C_{\text{in}} \times C_{\text{out}}$ on which Muon applies its orthogonalized momentum update in parallel.

These batched matrix layouts are critical for Muon: they expose the correct 2D structure to the optimizer without flattening across unrelated axes, preserve per-kernel/per-expert update geometry, and allow efficient fused batched Newton–Schulz steps. In practice, we use 5 Newton–Schulz iterations with Nesterov momentum for the internal SGD, following (Jordan et al., 2024).

A.11. Hyperparameter Ablations

In this section, we provide detailed ablation studies on hyperparameter choices that were explored during model development. While these experiments informed our final configuration, they represent implementation details rather than core conceptual contributions.

Table 11. Ablation of key sampling configurations. **Strategy** denotes point selection method (Full: all points, Random: random subset). **Cap Mode** controls when to limit sample size (Always: fixed limit, Train Only: limit during training only). **Update Mode** determines sampling frequency (Step: resample every decoder layer, Epoch: sample once per forward pass).

			Class Agnostic			200-Way Class Specific		
Strategy	**Cap Mode**	**Update Mode**	**AP**	**AP25**	**AP50**	**mAP**	**mAP25**	**mAP50**
Full	Always	Step	0.24039	0.67884	0.48610	0.08925	0.20947	0.15192
Full	Always	Epoch	0.23490	0.65596	0.46941	0.09867	0.22479	0.17256
Full	Train Only	Step	0.23384	0.65098	0.45943	0.09332	0.21709	0.16726
Full	Train Only	Epoch	0.23592	0.66030	0.47371	0.09167	0.22452	0.16596
Random	Always	Step	0.24028	0.66436	0.48141	0.09276	0.21519	0.16254
Random	Always	Epoch	0.24256	**0.68503**	0.48837	0.09418	0.22070	0.16201
Random	Train Only	Step	0.23211	0.65906	0.47518	0.09217	0.21420	0.16125
Random	Train Only	Epoch	**0.24615**	0.68180	**0.49060**	**0.10007**	**0.23347**	**0.17483**

Table 12. Ablation of normalization strategy for zero-shot 3D instance segmentation on ScanNet200 (validation). We train for 25k iterations with Muon (lr $2e{-3}$) using batch size 2 on 32 GPUs. For definition of the normalization strategies, see Section 11.

Method	mAP	mAP_{50}	mAP_{25}	mAP_{head}	$mAP_{com.}$	mAP_{tail}
SpaCeFormer (Default)	7.78	14.24	18.93	10.58	7.14	5.28
SpaCeFormer (PreNorm)	7.60	13.73	18.57	10.62	6.47	5.42
SpaCeFormer (PostNorm)	6.23	12.34	17.43	9.45	5.21	3.70

A.11.1. Sampling Strategy

Table 11 analyzes different key sampling strategies for the decoder. We find that **Random** sampling outperforms Full sampling, and applying a cap only during training (**Train Only**) yields better results than always capping. Furthermore, updating samples once per **Epoch** (forward pass) proves superior to re-sampling at every decoder step.

A.11.2. Normalization Strategy

We evaluate three normalization placement strategies: default normalization (as defined in Section A.4), pre-attention normalization, and post-attention normalization. Table 12 shows that post-attention normalization performs slightly better across all benchmarks, though differences are modest (within 0.5% mIoU). We use default normalization in our final model as it provides a good balance of performance and training stability.

A.11.3. Window Size Analysis

We further analyze which hierarchical levels should use window attention versus point-based Morton ordering. Table 13 shows results for different configurations. The configuration **Enc. + Dec. 64/48** where the highest and the second highest resolution layers of window size 64 and 48 respectively achieved the best performance, demonstrating that applying window attention at the finest hierarchical levels while using Morton ordering at coarser levels optimally balances local spatial locality with global scene structure.

A.12. Backbone Comparison and Configuration Analysis

We compare our Space-Curve Transformer backbone against the PTv3 baseline across four benchmarks, and analyze the effect of hidden dimension and window size configurations. Table 14 shows that Space-Curve Transformer consistently outperforms PTv3 across all benchmarks under identical training conditions (same optimizer, learning rate, batch size of 32 on 16 GPUs, 25k iterations). Increasing hidden dimension and adding spatial window attention at fine-grained levels further improves performance.

Table 13. Ablation of window sizes for zero-shot 3D instance segmentation on ScanNet200 (validation). We vary the window size configuration for the Encoder only, Decoder only, or both (Enc. + Dec.). When two window sizes are denoted (e.g., 64 / 48), they correspond to the window sizes for the finest (L1) and second finest (L2) hierarchies, respectively. We train for 25k iterations with Muon (lr 2e−3) using batch size 2 on 32 GPUs.

		Class Agnostic			200-Way Class Specific		
Module	**Win. Size**	**AP**	**AP25**	**AP50**	**mAP**	**mAP25**	**mAP50**
Encoder	32	0.23785	0.68051	**0.48933**	**0.10504**	0.23717	**0.18500**
Encoder	64	0.24273	**0.68163**	0.48702	0.09958	0.23536	0.17870
Encoder	128	0.23956	0.67103	0.48083	0.09648	0.22886	0.17206
Encoder	32 / 24	0.23904	0.67107	0.48086	0.10010	**0.23914**	0.17849
Encoder	64 / 48	**0.24629**	0.67780	0.48662	0.09657	0.23014	0.16899
Encoder	128 / 96	0.23392	0.67035	0.47444	0.09183	0.21528	0.16142
Decoder	32	0.24228	0.67949	0.48448	0.09612	0.22739	0.16881
Decoder	64	**0.24655**	0.68339	0.49284	0.09064	0.21653	0.16108
Decoder	128	0.24228	**0.68729**	**0.49285**	0.09999	**0.22970**	0.17504
Decoder	32 / 24	0.24299	0.67593	0.48244	0.09331	0.22171	0.16277
Decoder	64 / 48	0.24575	0.68258	0.48697	**0.10213**	0.22904	**0.17516**
Decoder	128 / 96	0.23770	0.67711	0.48474	0.09404	0.22491	0.17398
Enc. + Dec.	32	0.23624	0.66382	0.47006	0.09703	0.22197	0.16720
Enc. + Dec.	32 / 24	0.23908	0.66986	0.47967	0.10649	0.23082	0.18304
Enc. + Dec.	128	**0.25190**	0.68012	0.49562	0.09169	0.21653	0.16040
Enc. + Dec.	64	0.23878	0.67813	0.48443	0.10258	0.24082	0.18349
Enc. + Dec.	64 / 48	0.25178	**0.69114**	**0.50447**	**0.11092**	**0.24312**	**0.18783**
Enc. + Dec.	64 / 48 / 32	0.24670	0.68019	0.48613	0.10136	0.22797	0.17482
Enc. + Dec.	64 / 48 / 32 / 24	0.24224	0.68162	0.48716	0.10134	0.23662	0.17905
Enc. + Dec.	96 / 64	0.24377	0.68615	0.49529	0.09347	0.22416	0.16551
Enc. + Dec.	96 / 64 / 48	0.24308	0.68265	0.48681	0.10228	0.22966	0.17186
Enc. + Dec.	128 / 96	0.24416	0.68858	0.50031	0.09559	0.22862	0.17767

A.13. Class-Agnostic Instance Segmentation

Table 15 reports class-agnostic AP (mask quality independent of semantic labeling) on ScanNet++ and Replica. On ScanNet++, SpaCeFormer achieves 29.8 AP, outperforming MaskClustering (27.9 AP) despite using 3D-only input and no external proposals. More notably, our AP_{50} (54.8) and AP_{25} (75.1) substantially exceed all baselines, and our recall (74.7) nearly doubles that of Any3DIS (40.8). On Replica (zero-shot), SpaCeFormer achieves 33.2 AP with 69.8 recall, demonstrating strong cross-domain mask quality generalization.

A.14. Per-Class Confusion Matrix

We visualize the row-normalized confusion matrix (recall) for the best performing model in Figure 21. The diagonal dominance indicates strong performance across most categories, though some confusion persists between semantically similar classes such as table/desk and cabinet/shelves.

Table 14. Validation mIoU (%) on ScanNet20, ScanNet++, ScanNet200, and Matterport3D. We use the same optimizer, learning rate, batch size (32 on 16 GPUs), and trained for 25k iterations.

Method	ScanNet20	ScanNet++	ScanNet200	Matterport3D
PTv3	63.71	24.52	14.77	13.17
Space-Curve Transformer	**65.46**	**25.84**	**16.55**	**13.95**
Space-Curve Transformer + 256C	**65.46**	25.84	16.55	13.95
Space-Curve Transformer + 512C	63.28	25.68	16.9	13.74
Space-Curve Transformer + 768C	64.02	**27.00**	17.91	**15.13**
Space-Curve Transformer + 1024C	65.19	26.07	**18.12**	**15.13**
Space-Curve Transformer 512C + 16	**65.68**	25.81	16.57	13.87
Space-Curve Transformer 512C + 32	63.28	25.68	16.9	13.74
Space-Curve Transformer 512C + 64	63.67	26.42	17.49	**14.09**
Space-Curve Transformer 512C + 64 + 32	64.78	**26.92**	**17.52**	13.36
Space-Curve Transformer 512C + 64 + 64	65.08	26.10	17.25	13.52
Space-Curve Transformer 768C + 32	65.11	26.74	18.17	14.2
Space-Curve Transformer 768C + 64	**67.3**	28.13	19.04	13.93
Space-Curve Transformer 768C + 64,32	65.71	27.61	18.62	14.06
Space-Curve Transformer 768C + 64,48,32	65.14	**29.13**	18.82	14.27
Space-Curve Transformer 768C + 64,48,32,24	65.24	27.34	18.41	13.89
Space-Curve Transformer 768C + 64,48,32,24,16	66.4	28.15	18.59	**14.76**
Space-Curve Transformer 768C + 96	66.71	27.47	**19.47**	13.77
Space-Curve Transformer 1024C + 64	65.98	**28.56**	19.52	14.87
Space-Curve Transformer 1024C + 96	65.02	28.05	**19.94**	14.53
Space-Curve Transformer 1024C + 128	**66.32**	28.37	19.9	**15.18**

Table 15. **Class-agnostic instance segmentation on ScanNet++ and Replica.** AP evaluates mask quality independent of semantic labeling. ScanNet++ baselines from MaskClustering (Yan et al., 2024), Any3DIS (Lu et al., 2025), SAI3D (Yin et al., 2024), and SAM2Object (Jia et al., 2025). * uses closed-vocabulary Mask3D proposals trained with GT.

		ScanNet++ (100 classes)				**Replica (8 scenes)**			
Method	Input	AP	AP_{50}	AP_{25}	Recall	AP	AP_{50}	AP_{25}	Recall
SAI3D (2024)	3D+2D	17.1	31.1	49.5	–	–	–	–	–
OVIR-3D (2023)	3D+2D	19.4	34.1	46.5	–	–	–	–	–
SAM2Object (2025)	3D+2D	20.2	34.1	48.7	–	–	–	–	–
Any3DIS (2025)	3D+2D	22.2	35.8	47.0	40.8	–	–	–	–
OpenMask3D* (2023)	3D+2D	22.8	33.3	45.7	–	–	–	–	–
MaskClustering* (2024)	3D+2D	27.9	42.8	54.7	–	–	–	–	–
SpaCeFormer (Ours)	3D only	**29.8**	**54.8**	**75.1**	**74.7**	**33.2**	**56.1**	**68.7**	**69.8**

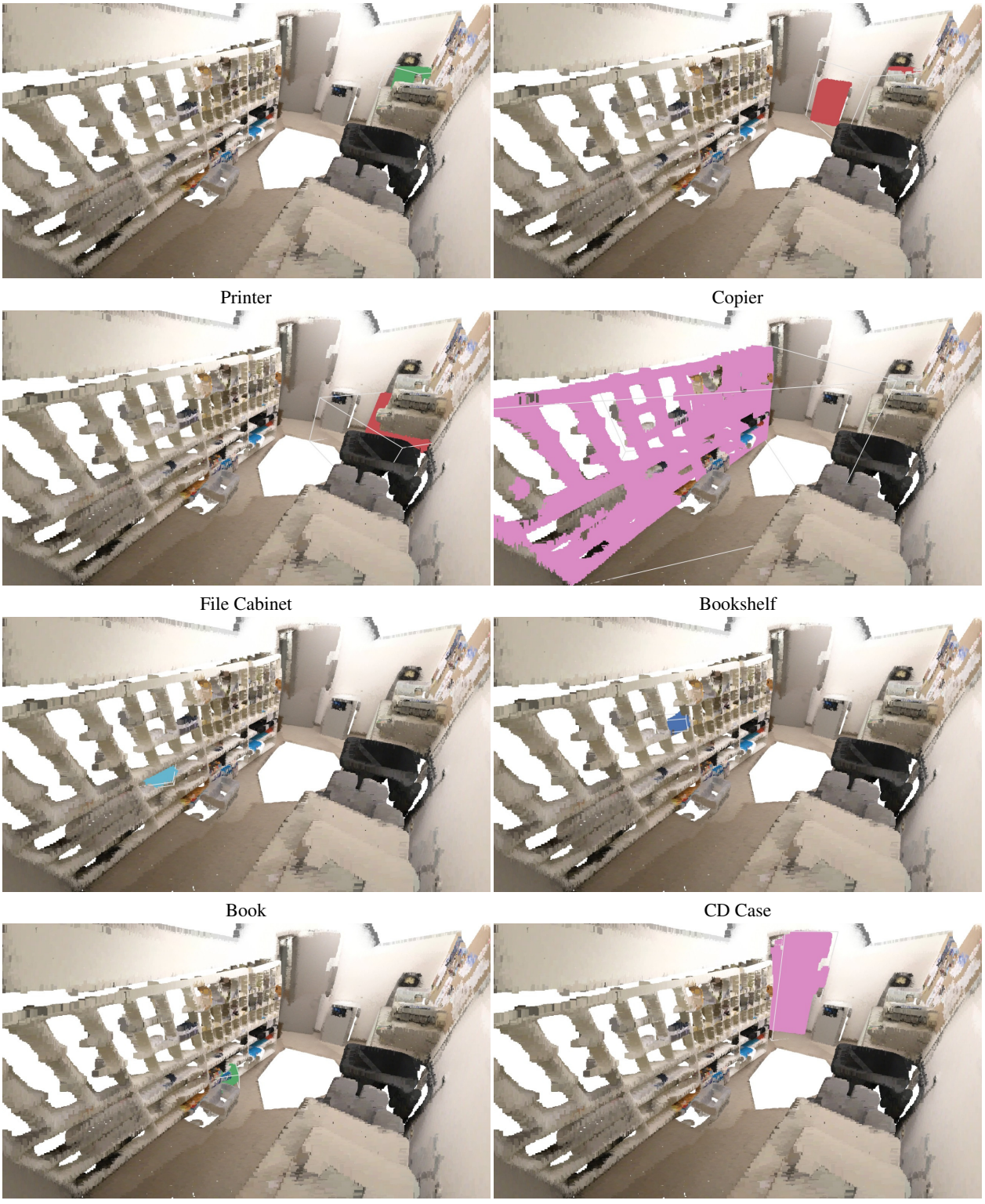

Figure 15. **Additional Qualitative Results (Scene 0462).** We show 3D mask predictions for the Copy Room scene, demonstrating segmentation of office equipment and furniture.

Recycling Bin

Rack

Cup

Bowl

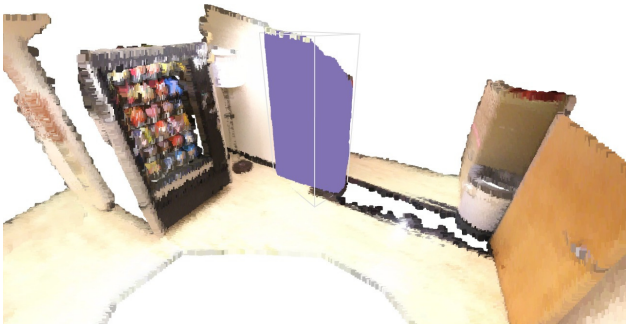

Board

Cup

Figure 16. **Additional Qualitative Results (Scene 0019).** We show 3D mask predictions for the Kitchenette scene, highlighting the ability to segment small objects like cups and bowls.

Figure 17. **Additional Qualitative Results (Scene 0474).** We show 3D mask predictions for the Office scene, including computer peripherals and furniture.

Ceiling Fan

Cistern

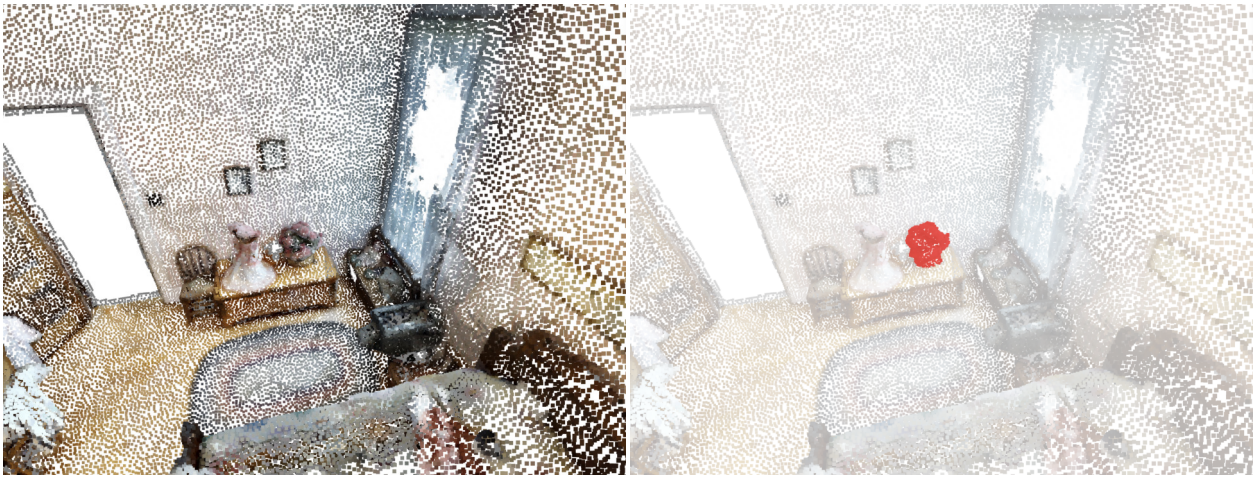

Flower

Figure 18. **Additional Novel Category Segmentation on Matterport3D (1/2).** We evaluate on categories absent from the ScanNet200 taxonomy. The left column shows the input point cloud, and the right column shows the predicted mask highlighted in red.

Globe

Sewing Machine

Stroller

Figure 19. **Additional Novel Category Segmentation on Matterport3D (2/2).** We evaluate on categories absent from the ScanNet200 taxonomy. The left column shows the input point cloud, and the right column shows the predicted mask highlighted in red.

Desk

Bookshelf

Refrigerator

Chair

Figure 20. **Missed Ground Truth Visualizations.** We visualize examples where the network predictions failed to achieve an IoU > 0.5. These cases include challenging instances such as partially occluded desks or geometrically complex bookshelves.

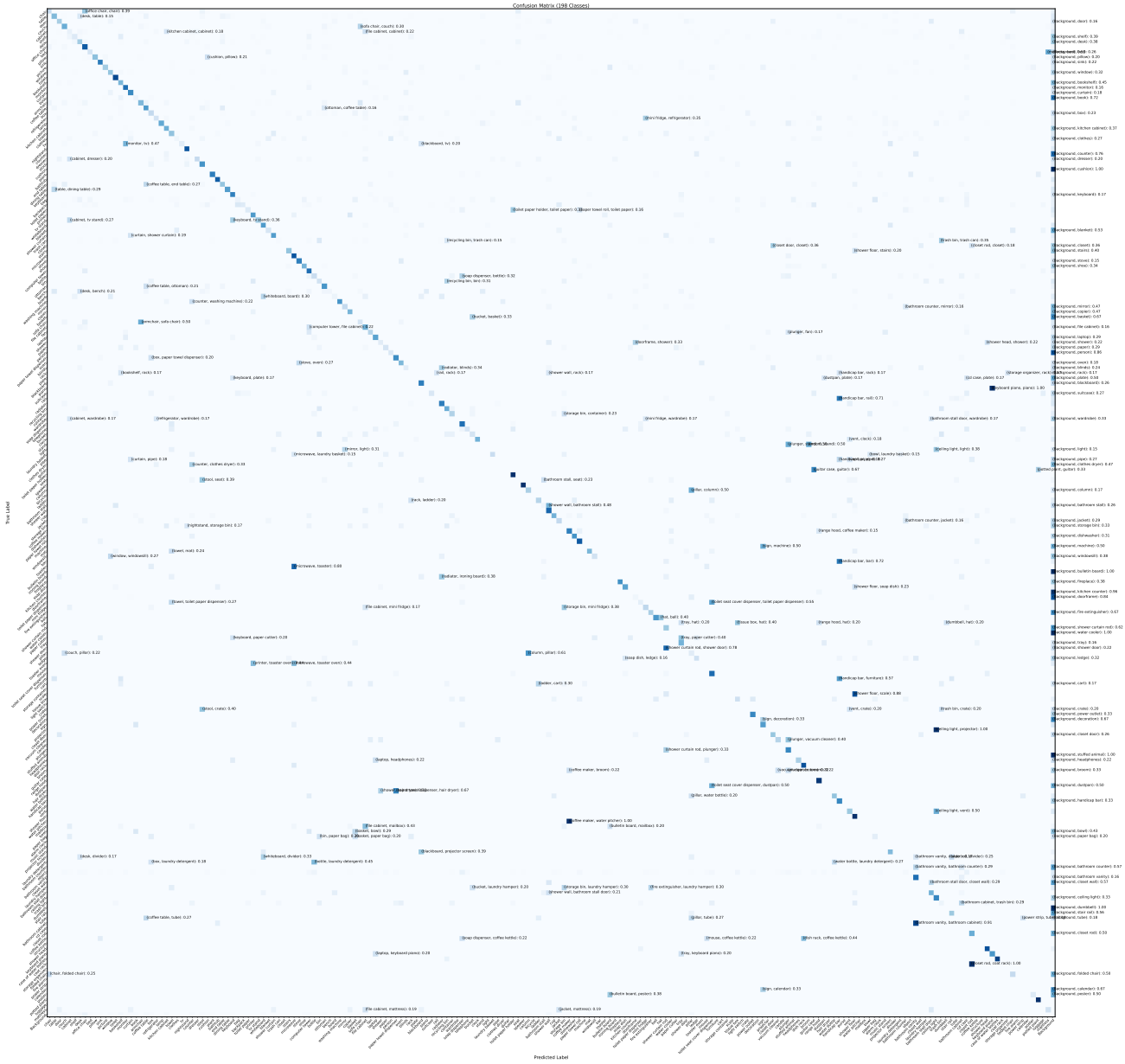

Figure 21. Confusion matrix of the validation set predictions. The values are row-normalized (recall). The model achieves high accuracy on distinct large objects (e.g., bed, wall, floor) but shows some confusion between geometrically similar categories.

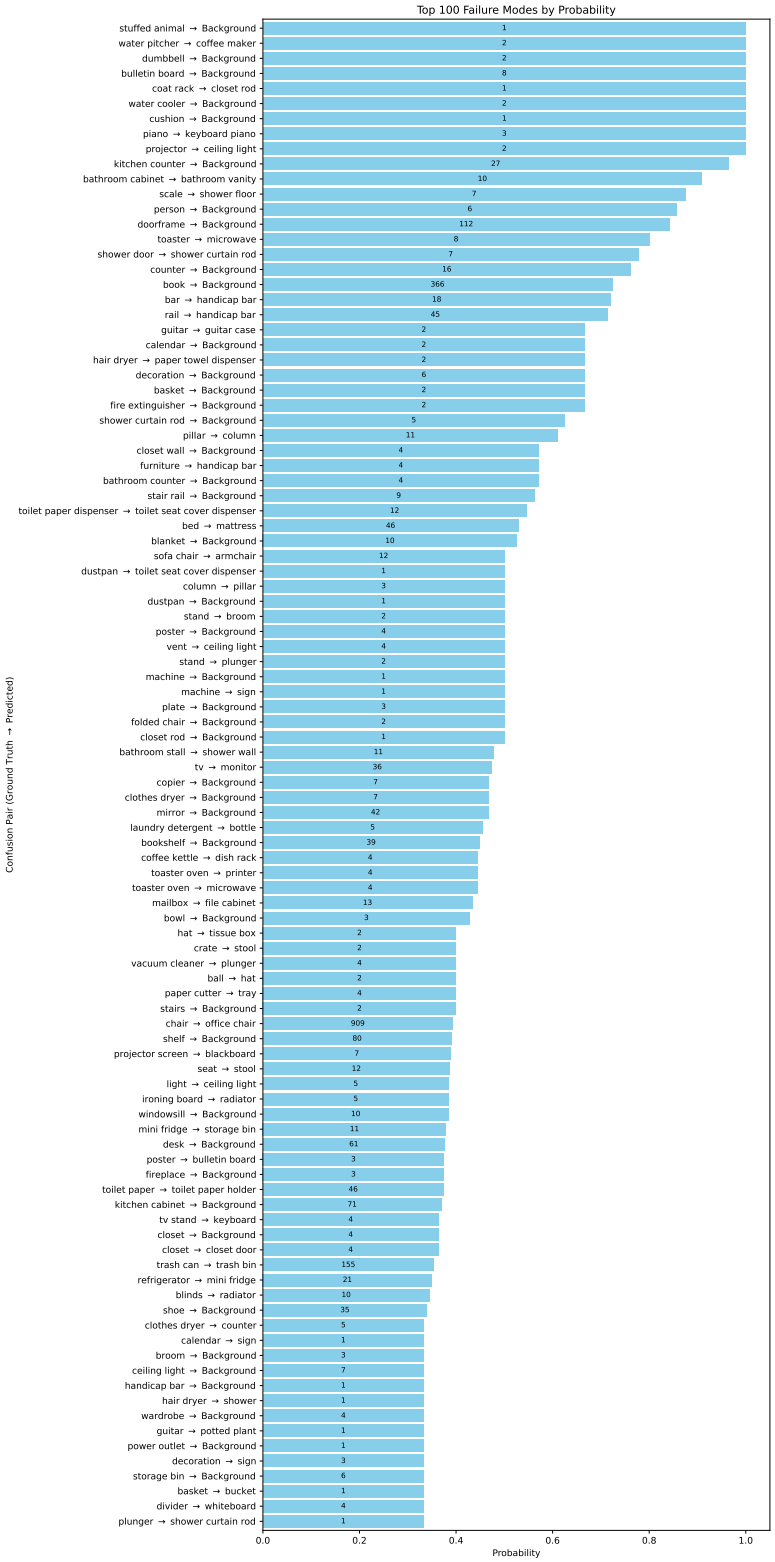

Figure 22. Top 100 most confused prediction pairs. The bar length represents the confusion probability, while the number inside each bar indicates the absolute count of failure cases. The y-axis labels show the Ground Truth → Prediction class assignments.